Contrib Mineral Petrol (2013) 166:861–886
DOI 10.1007/s00410-013-0920-3

ORIGINAL PAPER

Crystallization of oxidized, moderately hydrous arc basalt at mid- to lower-crustal pressures: implications for andesite genesis

Dawnika L. Blatter · Thomas W. Sisson · W. Ben Hankins

Received: 30 October 2012 / Accepted: 25 June 2013 / Published online: 22 August 2013
© Springer-Verlag (outside the USA) 2013

Abstract This study focuses on the production of convergent margin calc-alkaline andesites by crystallization–differentiation of basaltic magmas in the lower to middle crust. Previous experimental studies show that dry, reduced, subalkaline basalts differentiate to tholeiitic (high Fe/Mg) daughter liquids, but the influences of H_2O and oxidation on differentiation are less well established. Accordingly, we performed crystallization experiments at controlled oxidized fO_2 (Re–ReO_2 $\approx$ ΔNi–NiO + 2) on a relatively magnesian basalt (8.7 wt% MgO) typical of mafic magmas erupted in the Cascades near Mount Rainier, Washington. The basalt was synthesized with 2 wt% H_2O and run at 900, 700, and 400 MPa and 1,200 to 950 °C. A broadly clinopyroxenitic crystallization interval dominates near the liquidus at 900 and 700 MPa, consisting of augite + olivine + orthopyroxene + Cr-spinel (in decreasing abundance). With decreasing temperature, plagioclase crystallizes, Fe–Ti-oxide replaces spinel, olivine dissolves, and finally amphibole appears, producing gabbroic and then amphibole gabbroic crystallization stages. Enhanced plagioclase stability at lower pressure narrows the clinopyroxenitic interval and brings the gabbroic interval toward the liquidus. Liquids at 900 MPa track along Miyashiro's (Am J Sci 274(4):321–355, 1974) tholeiitic versus calc-alkaline boundary, whereas those at 700 and 400 MPa become calc-alkaline at silica contents $\geq$56 wt%. This difference is chiefly due to higher temperature appearance of magnetite (versus spinel) at lower pressures. Although the evolved liquids are similar in many respects to common calc-alkaline andesites, the 900 and 700 MPa liquids differ in having low CaO concentrations due to early and abundant crystallization of augite, with the result that those liquids become peraluminous (ASI: molar Al/(Na + K + 2Ca) > 1) at $\geq$61 wt% SiO_2, similar to liquids reported in other studies of the high-pressure crystallization of hydrous basalts (Müntener and Ulmer in Geophys Res Lett 33(21):L21308, 2006). The lower-pressure liquids (400 MPa) have this same trait, but to a lesser extent due to more abundant near-liquidus plagioclase crystallization. A compilation of >6,500 analyses of igneous rocks from the Cascades and the Sierra Nevada batholith, representative of convergent margin (arc) magmas, shows that ASI increases continuously and linearly with SiO_2 from basalts to rhyolites or granites and that arc magmas are not commonly peraluminous until SiO_2 exceeds 69 wt%. These relations are consistent with plagioclase accompanying mafic silicates over nearly all the range of crystallization (or remelting). The scarcity of natural peraluminous andesites shows that progressive crystallization–differentiation of primitive basalts in the deep crust, producing early clinopyroxenitic cumulates and evolved liquids, does not dominate the creation of intermediate arc magmas or of the continental crust. Instead, mid- to upper-crustal differentiation and/or open-system processes are critical to the production of intermediate arc magmas. Primary among the open-system processes may be extraction of highly evolved (granitic, rhyolitic) liquids at advanced degrees of basalt solidification (or incipient partial melting of predecessor gabbroic intrusions) and mixing of such liquids into replenishing basalts. Furthermore, if the andesitic-composition continents derived from basaltic sources, the arc

Communicated by G. Moore.

D. L. Blatter (✉) · T. W. Sisson · W. B. Hankins
Volcano Science Center, United States Geological Survey, 345 Middlefield Road, Menlo Park, CA 94025, USA
e-mail: dblatter@usgs.gov

ASI–SiO_2 relation shows that the mafic component returned to the mantle was gabbroic in composition, not pyroxenitic.

Keywords Experiments · Calc-alkaline basalt · Andesite genesis · Basalt fractionation

Introduction

The origins of tholeiitic versus calc-alkaline andesites are enduring issues in geochemistry mainly because the continents have calc-alkaline andesite or dacite average compositions (Rudnick and Gao 2003), whereas calc-alkaline intermediates are unknown from intraplate ocean island and mid-ocean ridge settings. Several studies have proposed that magnesian andesites (MgO $\geq \sim 6$ wt%) and basaltic andesites (MgO $\geq \sim 8$ wt%) are direct peridotite partial melts (Kushiro 1974; Ringwood 1974; Kelemen 1986; Blatter and Carmichael 2001; Grove et al. 2003) or are reaction products of slab-derived fluids/melts and mantle harzburgite (Straub et al. 2008, 2011). Other studies infer that andesites and dacites with high Sr/Y ratios (adakites) may be partial melts of subducting oceanic lithosphere (Kay 1978; Stern and Kilian 1996; Martin et al. 2005), of foundering continental roots, or form by deep crystallization–differentiation involving garnet (Macpherson et al. 2006).

Common arc andesites, however, are not high in MgO or Sr/Y (Gill 1981; Thorpe 1982). Instead, they are widely associated with basalts, and within whole arcs, andesites form an intermediate member in a continuous compositional spectrum spanning from basalt to rhyolite or rhyodacite (and their intrusive equivalents). This association and compositional continuity with basalt, as well as other petrologic factors such as intermediate temperatures inferred for andesites, support the classical interpretation that most derive by crystal–melt separation processes from basaltic parents (Bowen 1928; Gill 1981; Sisson and Grove 1993a). Such derivation may include mixing between mafic replenishments and variably evolved differentiates or partial melts from earlier intrusions (Sakuyama 1981), as well as by conventional progressive crystallization–differentiation. Moderate assimilation of unrelated crustal rocks or their partial melts is also commonly documented (DePaolo 1980, 1981).

While geologic and petrologic evidence is strong for derivation of many andesites from basalts, it remains unclear why some andesites are calc-alkaline and others tholeiitic, and why calc-alkaline compositions dominated during continental growth. One position is that tholeiitic andesites are the normal crystallization–differentiation products of arc basalts, whereas calc-alkaline andesites result by mixing or assimilation of evolved crustal materials into basalt (Tatsumi 2005). On the other hand, it has been shown experimentally that elevated dissolved H_2O concentrations promote calc-alkaline differentiation of moderately oxidized basalts by lowering the crystallization temperatures of silicates more than those of FeTi oxides (Sisson and Grove 1993a; Botcharnikov et al. 2008; Tatsumi and Suzuki 2009). Highly evolved calc-alkaline differentiates (or partial melts) can also form from low-H_2O basalts (1.7–2.3 wt%), if the basalts are sufficiently oxidized (>Ni–NiO); if reduced, these basalts produce tholeiitic advanced differentiates (Sisson et al. 2005). A long-predicted association between oxidation state and tholeiitic versus calc-alkaline character (Osborn 1959) is supported by FeTi oxide-determined fO_2 and compositions of evolved volcanic rocks (Sisson et al. 2005), such that samples with $fO_2 >$ Ni–NiO + 0.5 ($\log_{10}$ units) plot chiefly in Miyashiro's (1974) calc-alkaline field, those with fO_2 <Ni–NiO-0.5 plot in the tholeiitic field, and those with fO_2 =Ni–NiO $\pm$ 0.5 straddle the tholeiitic–calc-alkaline boundary. Thus, fO_2 near that of the Ni–NiO buffer may be a critical boundary between calc-alkaline and tholeiitic differentiation paths. Considerable uncertainty remains, however, regarding the origins of calc-alkaline andesites because (1) elevated H_2O concentrations and oxidation states appear correlated (Carmichael 1991; Zimmer et al. 2010) obscuring their relative importance, (2) the fO_2 recorded by intermediate and evolved magmas may result from crustal-level processes and might not be representative of primitive basalts (Lee et al. 2005), and (3) primitive arc basalts, and their intrusive gabbroic equivalents, are uncommon in the upper crust, indicating that processes in the mid- to lower crust dominate transformations to andesite. To date, few experiments have been performed on hydrous basalts at deep-crustal conditions with oxidation states buffered at values potentially appropriate for calc-alkaline differentiation.

To advance the understanding of the potential origins of calc-alkaline andesites, we performed crystallization experiments at 900, 700, and 400 MPa on a relatively magnesian basalt (MgO = 8.7 wt%) typical of those erupted in the Quaternary from the Cascade magmatic arc near Mount Rainier, Washington (USA). The basaltic starting material was prepared with 2 wt% H_2O, near the lower limit of common arc basaltic melt inclusions (Métrich and Wallace 2008; Kelley and Cottrell 2009), but at the high end of dissolved H_2O values for back-arc basin basalts (Stolper and Newman 1994). Oxidation state was controlled near the Re–ReO_2 buffer (=Ni–NiO +1.7 to +2.0 $\log_{10}$ units) using a modified double-capsule configuration (Eugster 1957). This buffer was employed because it is close to but greater than the apparent $\sim$Ni–NiO oxidation divide for calc-alkaline versus tholeiitic differentiation and is within the oxidation range of common arc magmas as

indicated by their whole-rock ferric/ferrous ratios (Carmichael 1991), as well as numerous FeTi oxide determinations (Sisson et al. 2005).

Fundamental results of these experiments are that the elevated SiO_2 and modest FeO*/MgO of calc-alkaline andesites and dacites are readily produced by crystallization–differentiation of oxidized, moderately hydrous basalt at deep to mid-crustal pressures, but that the higher-pressure liquids, including those produced in other studies of deep basalt crystallization, differ from common andesites in important compositional aspects. These differences imply that progressive crystallization–differentiation from basalt at lower crustal depths may not act alone to produce calc-alkaline andesite. Other processes, notably deep-crustal mixing with evolved residual liquids and (or) with low-degree partial melts of predecessor intrusions may be more pervasive than is widely appreciated.

Experimental and analytical methods

Starting material

The investigated sample (01SB872) was collected from a basaltic lava flow at Paradise Falls (latitude 46.2292, longitude −121.9933), Washington, and is typical of the regional mafic volcanism in the vicinity of Mount Rainier, as well as of relatively primitive basalts found elsewhere in the Cascades magmatic arc (USA) (Bacon et al. 1997) (Table 1). Along with its high MgO content (8.66 wt%) and Mg# {100 × molar [MgO/(MgO + FeO*)]} of 65, the basalt also has moderately high Ni (161 ppm) and Cr (344 ppm) and no petrographic evidence of contamination, indicating that this composition is not far removed from that of a primary mantle melt. A moderate H_2O concentration was chosen to help isolate the relative effects of H_2O and fO_2 on differentiation behavior. The initial intent was to prepare a starting material with 3 wt% dissolved H_2O, but due to errors with H_2O concentration measurements early in the project, starting material with 2.1 ± 0.1 wt% H_2O was produced, as verified by later Fourier transform infrared (FTIR) spectroscopic determinations (Lowenstern and Pitcher 2013). Compilations of basaltic melt inclusions (Métrich and Wallace 2008) show that dissolved H_2O concentrations range between <1 and 5.2 wt% for arc basalts with >5 wt% MgO, and H_2O determinations for Cascades basaltic melt inclusions are generally toward the lower end of this range (Ruscitto et al. 2010; Shaw et al. 2011; Sisson and Layne 1993).

In order to avoid potential variability of H_2O between runs due to imprecise weighing and H_2O loss during welding, the starting material was prepared by dry grinding of nominally dry rock powder with hydrated glass produced by fusing the rock powder at 200 MPa H_2O-saturated in a rapid-quench zirconium-hafnium-molybdenum pressure vessel, using methods similar to those of Sisson and Grove (1993a) (details: $Au_{75}Pd_{25}$ capsule, Mt-Hem buffer, 1,290 °C, 30 min fusion). Mixing proportions were determined by measuring the H_2O concentrations in the hydrated glass and in the nominally dry rock powder by transmission FTIR on glass wafers. For the nominally dry rock powder, this involved rapidly fusing an aliquot in the piston cylinder press (900 MPa, 1,350 °C, 10 min), quenching to a glass, and analyzing by FTIR. The H_2O of the resulting mechanical mix was then verified by similar rapid fusions of aliquots and FTIR determinations (both replicated), yielding a final 2.1 ± 0.1 wt% H_2O. Although CO_2 was not intentionally added to the starting material, it was always found (650 ± 70 ppm, Table 2) during FTIR analysis of glasses synthesized in the piston cylinder and likely comes from use of a carbon-electrode arc welder to seal capsules.

Table 1 Normalized anhydrous starting composition: 01SB-872

	XRF[a]	XRF[b]	EPA[c]	EPA[d]
SiO_2	49.9	49.9	49.9 (2)[e]	50.3 (4)
TiO_2	1.25	1.26	1.32 (12)	1.19 (9)
Al_2O_3	17.0	17.0	17.2 (1)	17.1 (4)
FeO_T	9.28	9.19	9.54 (13)	9.31 (17)
MnO	0.16	0.16	0.18 (4)	0.16 (5)
MgO	8.67	8.76	8.31 (14)	8.27 (14)
CaO	10.0	10.1	10.1 (1)	10.1 (1)
Na_2O	3.02	3.07	2.86 (10)	2.92 (21)
K_2O	0.49	0.50	0.52 (2)	0.48 (3)
P_2O_5	0.22	0.19	0.17 (4)	0.18 (4)

[a] X-ray fluorescence analysis, USGS given in wt%

[b] X-ray fluorescence analysis, Washington State University, given in wt%

[c] Electron microprobe analysis of SB-872 nominally dry glass fused at 900 MPa and 1,350 °C for 10 min. Average of 18 analyses from center of sample to avoid areas of Fe loss near capsule edges

[d] Electron microprobe analysis of superliquidus experiment 2371 run at 700 MPa and 1,250 °C for 8 h. Average of 26 analyses from over the entire sample area

[e] One standard deviation of replicate analyses in terms of least cited units

FTIR methods

The dissolved H_2O and CO_2 concentrations of glasses synthesized as starting materials, and one experimental run product, were determined on doubly polished wafers by transmission FTIR using a Nicolet iN10 infrared imaging microscope with an attached liquid-N_2-cooled MCT-B detector at the USGS in Menlo Park, CA. For starting

Table 2 Transmission FTIR H_2O and CO_2 concentrations of starting material and experimental glass

Sample	t^a (μm)	t^b (μm)	ρ^c (kg/m^3)	A^{d}5200	A4500	A3550	A1635	A1515	A1435	H_2O^a (wt%)	H_2O^b (wt%)	CO_2 (ppm)
01SB-872 (20)[e]	64		2,808	0.0038	0.0086	1.283	0.183	0.086	0.087	1.95 (6)[f]	2.05 (10)	646 (66)
2351 (6)	152	42	2,792	0.0082	0.0018	0.840	0.303	0.203	0.203	1.89 (4)	1.99 (4)	639 (16)

[a] Thickness used and H_2O concentration calculated from combined 5200 and 4500 peaks

[b] Thickness used and H_2O concentration calculated from the 3550 peak

[c] Density of room temperature glass calculated using the model of Ochs and Lange (1999)

[d] Absorbance measured at each indicated band

[e] Number of analyses

[f] One standard deviation of replicate analyses in terms of least cited units

material glasses, a 150-μm, square aperture defined the analytical area, collecting 256 scans per area at 4 cm^{-1} wavenumber resolution. For run product glass, apertures were set as necessary to avoid crystals. IR absorption spectra were collected between 700 and 6,000 cm^{-1}. Two glass fragments from each aliquot of hydrated glass were polished and analyzed by collecting spectra across three lines of five points each and averaging the results. Concentrations of H_2O and CO_2 were calculated using Beer's law: $c = MA/\rho d\varepsilon$, where M is the molecular weight of H_2O or CO_2, A is the absorbance value measured for each peak, ρ is the density of 01SB872 glass at room temperature calculated using the density model of Ochs and Lange (1999), with H_2O calculated iteratively, d is the thickness of the glass wafer, measured by digital micrometer and by the specular reflectance interference fringe method (Wysolcazanski and Tani 2006) at the same locations as the analyses, and ε is the molar absorption coefficient, calculated as described following. Depending on the H_2O concentration and thickness of each wafer, various peaks and combinations of peaks could be quantified (Table 2). The broad, asymmetric peak at ~3,550 cm^{-1} was used to determine total H_2O (molecular H_2O and OH^-) where possible, with a molar absorptivity of 63 ± 3 L mol^{-1} cm^{-1} (Dixon et al. 1995), and a straight baseline. However, if the height of the 3,550 cm^{-1} peak exceeded 1.0 absorption unit, the near-IR peaks at 5,200 cm^{-1} (molecular H_2O) and 4,500 cm^{-1} (OH^-) were used. The molar absorptivities were calculated for each of these peaks based on the major element composition of the glass and the equations of Dixon et al. (1995). Values for these are as follows: 0.69 L mol^{-1} cm^{-1} for the 5,200 cm^{-1} peak, 0.54 L mol^{-1} cm^{-1} for the 4,500 cm^{-1} peak, and 25.1 L mol^{-1} cm^{-1} for the 1,635 cm^{-1} peak. The background curves for the 5,200 and 4,500 cm^{-1} peaks were hand-drawn using French curves. Heights of all peaks were measured manually. CO_2 concentrations were calculated using the carbonate peaks at 1,515 and 1,435 cm^{-1}, with molar absorptivity of 330 L mol^{-1} cm^{-1} (Dixon and Pan 1995). Thickness, density, absorbances, and H_2O and CO_2 concentrations are given for each sample in Table 2, along with 1σ uncertainties.

The attenuated total reflectance method (Lowenstern and Pitcher 2013) was applied to several run product glasses to measure their dissolved H_2O concentrations. This method uses a Ge ATR accessory crystal, with a refractive index of 4.0, to measure the evanescent wave absorption by H_2O and has been calibrated using basalt through rhyolite glasses with known H_2O concentrations, yielding $c = (\omega \times A_{3450}/\rho) + b$, where $\omega = 546 \pm 15$ (units: wt% cm^3/g), ρ = glass density (g/cm^3), $b = -0.19 \pm 0.03$ (wt%), and A_{3450} is the ATR absorbance (dimensionless) at 3450 cm^{-1} (Lowenstern and Pitcher 2013). This method is optimal for partly crystalline run products because it allows analysis of H_2O in singly polished samples with spot size down to 15 μm, and light penetration limited to ~1 micron below the surface. The aperture size for each sample was adjusted to the size of the melt pools (100 μm for the glassy samples to 30 μm for crystalline samples). Spectra were collected from 4,000 to 1,200 cm^{-1} with 256 scans for each spot and spectral resolution of 8 to 16 cm^{-1}, using the same Nicolet iN10 and detector described above. A reference spectrum was collected in air before each sample spot, and a straight baseline was used to determine the height of the 3,450 cm^{-1} band. Several spots were analyzed in broadly distributed locations across each sample and averaged to derive the H_2O concentrations and 1σ uncertainties (Table 3).

Precautions against Fe loss

All experiments were run in 3 mm $Au_{75}Pd_{25}$ capsules with $Au_{80}Pd_{20}$ lids in a "trash can" (flat-ended cylinder) configuration (Fig. 1). A preliminary experimental series was performed at 900 MPa and Re–ReO_2 in untreated capsules.

Table 3 ATR-FTIR H_2O concentrations of experimental glass

Sample	ρ[a] (kg/m^3)	A[b]3550	H_2O (wt%)
2351 (10)[c]	2,792	0.0113	2.01 (2)[d]
2362 (10)	2,768	0.0127	2.31 (2)
2353 (9)	2,746	0.0131	2.42 (4)
2354 (9)	2,720	0.0153	2.87 (5)
2363 (8)	2,713	0.0154	2.91 (6)
2356 (9)	2,686	0.0163	3.12 (8)
2357 (19)	2,647	0.0178	3.49 (10)
2359 (11)	2,612	0.0189	3.76 (10)
2360 (8)	2,555	0.0203	4.15 (21)
2358 (6)	2,535	0.0228	4.74 (12)
2364 (6)	2,499	0.0205	4.30 (11)
2371 (10)	2,794	0.0117	2.10 (2)
2369 (9)	2,799	0.0119	2.14 (2)
2379 (10)	2,730	0.0140	2.61 (6)
2374 (26)	2,662	0.0174	3.37 (6)
2388 (20)	2,592	0.0184	3.69 (10)
2387 (7)	2,525	0.0204	4.21 (12)
2376 (6)	2,494	0.0177	3.69 (17)
2384 (9)	2,774	0.0128	2.32 (2)
2389 (9)	2,753	0.0134	2.47 (5)
2391 (14)	2,665	0.0166	3.21 (6)
2380 (26)	2,642	0.0170	3.33 (7)
2390 (11)	2,543	0.0188	3.84 (12)
2381 (12)	2,490	0.0202	4.24 (7)

[a] Density of room temperature glass calculated using the model of Ochs and Lange (1999)

[b] Band of measured absorbance

[c] Number of analyses

[d] One standard deviation of replicate analyses in terms of least cited units

Due to relatively high fO_2, samples run for 8 h between 1,135 and 1,185 °C only lost between 1 and 8 relative percent Fe, with a positive correlation between temperature and the amount of Fe lost to the capsule. Although this amount of Fe loss is small, it caused small but detectable Fe depletions in the glass adjacent to the capsule walls. Therefore, the majority of syntheses were in capsules pre-treated with Fe to further minimize Fe losses, including repeats of many 900 MPa runs. The optimal Fe concentration for the runs was determined by short-duration whole fusions of the starting material at 900 MPa and Re–ReO_2 in untreated AuPd capsules and then analyzing Fe in the inner rim of the sample capsule by electron microprobe. Preparation of capsules with this Fe concentration ($\sim$1.8 mol%) was then attempted by equilibrating with pure magnetite at 1,100 °C, 1 bar, and fO_2 determined from the equilibrium constant for the reaction: $Fe_3O_4 = 3Fe^{\circ} + 2O_2$ (from the fO_2 expressions for the wüstite–magnetite and iron–wüstite buffers tabulated by Chou (1978)), and the Fe in AuPd activity model of Balta et al. (2011). Pre-treatment was achieved by packing and immersing the capsules in a 2:1 wt. mixture of Fe_3O_4 (Aldrich) and a commercial clear jewelry enamel designed to wet Au-rich alloys, while held in a Pt crucible suspended in a Deltec 1-atm gas-mixing furnace. Oxygen fugacity of the furnace was controlled at -7.64 ($\log_{10}$), using CO_2–ArH_2 gas mixture, measured with a ZrO_2 electrolyte fO_2 sensor. Temperature was set at 1,100 °C using a Eurotherm controller and measured with a $Pt/Pt_{10}Rh$ thermocouple, calibrated to the melting temperature of gold. Capsules and lids were pre-treated in batches of four and held at conditions for $\sim$1 week to ensure sufficient Fe saturation into the AuPd alloys. The pre-treated capsules and lids were then cleaned of all magnetite by chipping out the brown glassy coating and then heating in concentrated HF in a sealed Teflon "Parr" bomb in a box furnace at 120 °C for several days. HF-cleaned capsules and lids were then rinsed in cold dilute HCl and then in deionized water in an ultrasonic bath to remove any residues. Slices of some pre-treated capsules were then analyzed by electron microprobe to determine the levels of Fe saturation. Fe concentrations were about half the intended values, probably due to inaccuracy in the Fe activity model extrapolated to very low concentrations. With this method the greatest apparent Fe loss to a pre-saturated capsule was calculated at 1.9 relative percent in our hottest experiment: 2371, run at 1,200 °C for 8 h, which was deemed acceptably low. Valuable lessons were that starting with Fe metal and pre-treating at high temperature (>1,200 °C) produced brittle capsules, that open cylinders are much easier to clean than those with a lid welded into one end prior to Fe saturation, and that HCl should not be added to the HF dissolution step (dissolves Pd).

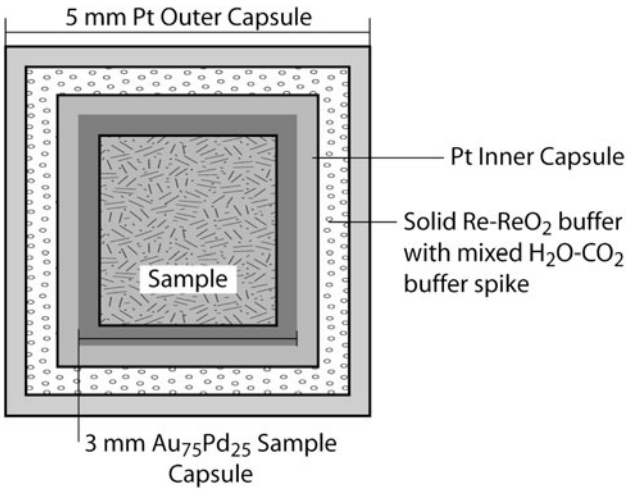

Fig. 1 Schematic of double-capsule configuration

Sample loading and fO_2 buffering

In order to buffer fO_2 at H_2O undersaturated conditions, it was necessary to modify the classic double-capsule technique of Eugster (1957). Prior to use, the 3-mm $Au_{75}Pd_{25}$ capsules (initially pure, later Fe-saturated) were sheathed in snug fitting thin-walled Pt to prevent Au–Re eutectic melting (Fig. 1). A cup-shaped $Au_{80}Pd_{20}$ lid (initially pure, later Fe-saturated) was pressed into one end of the sheathed capsule, along with a close fitting outer Pt wafer, trimmed, and arc welded in place. The capsule was then packed with 35 mg of the prepared starting material, and a similar lid with Pt wafer was pressed into and welded to seal the open end. The Pt-sheathed inner capsules were then loaded into 5-mm-diameter Pt outer capsules, separated by ~175 mg of high-purity 50 % Re and 50 % ReO_2 powder, plus an H_2O–CO_2 vapor source, described following, and sealed by welding a Pt lid. Sealed double capsules were then gently compressed to a uniform length (5 ± 0.25 mm) and right cylindrical shape with a die and vise.

Because the samples were H_2O undersaturated, vapor in the buffer assemblage was prepared as a mixed-volatile (H_2O–CO_2) spike (~10 mg) tailored to the approximate fH_2O of the molten starting material at each pressure. The fH_2O of fully molten sample was estimated with the H_2O–CO_2 solubility model of Papale et al. (2006) at the pressures of interest and the liquidus temperature using the initially intended 3 wt% H_2O, with CO_2 increased numerically until the melt was predicted to saturate with a trace (<0.1 wt%) of H_2O–CO_2 vapor. The composition of this fictive saturating H_2O–CO_2 vapor, provided by the Papale et al. (2006) model, gives an estimate of the fH_2O of the sample and was reproduced by mixing appropriate amounts of $Mg(OH)_2$ and $MgCO_3$ into the Re–ReO_2 buffer powder. Strictly, this vapor composition would match the fH_2O of the sample (with 3 wt% dissolved H_2O) only when the sample is wholly molten, whereas with crystallization of anhydrous minerals, the fH_2O of the sample rises relative to that of the buffer, increasing fO_2 of the sample relative to the buffer. The fO_2 of the sample, relative to that of the buffer, is given by the square of the ratio of $fH_2O_{sample}/fH_2O_{buffer}$. Because it was subsequently determined that the starting material contained 2 wt% H_2O, experimental fO_2s were recalculated and were about 0.5 $\log_{10}$ units low relative to the intended values, as explained in the "Results" section.

At the end of each run, the buffer materials were mounted in epoxy, polished, and analyzed by electron microprobe energy dispersive spectroscopy (EDS) to confirm that both Re and ReO_2 remained. Pure Re metal and ReO_2 were identified in the used buffer materials, but Re also alloyed with the Pt of the inner sheath and outer capsule to some extent in all of the runs, thus providing a limiting lower value for the activity of the Re in the buffer. Based on microprobe analyses of the Pt–Re capsules from runs at a wide variety of run conditions (995–1,185 °C and 8–96 h), the composition of the alloy varied from 24 to 54 mol% Re, to pure Re coexisting with ReO_2. Since the Re–Pt system produces a symmetric miscibility gap (Hansen and Anderko 1958), the reduction in the activity of Re can be calculated (Wood and Fraser 1976) and its effect on the fO_2 of the run would result in an increase in the fO_2 of the run by only 0.06 to 0.10 log units.

Experimental setup

Experiments at 900, 700, and 400 MPa were run in a 2.54-cm, end-loaded, solid-media piston cylinder (similar to: Boyd and England 1960) at the USGS in Menlo Park, CA, using graphite furnaces and pressed CaF_2 assemblies. Capsules were run with a vertical axis, parallel to the graphite furnace bore, with the sample centered in the furnace hot spot. The control thermocouple (S-type: Pt–Pt_{90}–Rh_{10}) was positioned on the top end of the outer capsule, with a temperature offset (6–10 °C) between the control thermocouple and the hot spot, as determined by prior thermal gradient measurements at P and T using multiple-junction thermocouples (smaller offsets at lower temperatures); reported temperatures are those extrapolated for the hot spot. Assemblies were initially pressurized to near the desired run pressure (measured by digital Heise gauge), and temperature was then ramped up at ~99 °C per minute to approximately the liquidus of the sample, held for 30 min, and then reduced to the intended run temperature, at which time the pressure was adjusted to the intended value. Small pressure adjustments were then made during the run, as needed, to keep the sample pressure within 2.5 MPa of the intended value. Sample temperature generally did not require adjustment and varied by less than ±2 °C from the value set on the Eurotherm controller. Sample pressure was calibrated for this assembly type using the CsCl melting technique (Bohlen and Boettcher 1982) and is reproducible within 2.5 MPa through the use of an argon reservoir connected to the hydraulic line and by pre-compressing CaF_2 furnace parts in a 2-ton press (Sisson et al. 2005). Run durations varied with temperature. High-temperature experiments were brief (~8 h) to avoid exhausting the Re–ReO_2 buffer, and lower-temperature runs were up to 99 h to ensure sufficient time to approach equilibrium (Table 4).

Electron microprobe analytical conditions

Sample capsules from each run were sectioned, mounted in epoxy, and polished for microanalysis. Buffer assemblies were assessed for the presence of both Re and ReO_2 by

Table 4 Experimental conditions and assemblages

Run #	T (°C)	t (hours)	Capsule[a]	Phases (modes)[b]	Σr^2	$K_D(Fe^{2+}–Mg)$[c] Olv-liq	$K_D(Fe^{2+}–Mg)$[c] Cpx-liq	$K_D(Ca–Na)$[d] Plag-liq	H_2O (wt%)[e] Vapor	CO_2 (wt%)[e] Vapor	$\Delta ReReO_2$[f]
P = 900 MPa											
2364	975	99	No	Gl(20), Cpx(13), Opx(3), Pl(23), Hbl(40), Mt(1)	0.09	–	0.28	1.18	–	–	1.1
2358	995	96	No	Gl(18), Cpx(12), Opx(9), Pl(26), Hbl(35), Mt(tr)	0.08	–	0.32	1.29	–	–	1.2
2360	1,015	96	No	Gl(22), Cpx(15), Opx(10), Pl(22), Hbl(31), Mt(tr)	0.04	–	0.31	1.49	–	–	0.9
2359	1,035	72	No	Gl(33), Cpx(16), Opx(9), Pl(19), Hbl(22), Mt(1)	0.02	–	0.36	1.49	–	–	0.6
2357	1,055	15	No	Gl(60), AlSp(3), Cpx(28), Opx(6), Pl(3)	0.00	–	0.32	1.60	–	–	0.0
2356	1,075	15	No	Gl(64), AlSp(2), Cpx(27), Opx(7), Pl(tr)	0.08	–	0.31	1.61	–	–	0.0
2363	1,095	15	Yes	Gl(68), Olv(tr), AlSp(2), Cpx(24) Opx(6), Pl(tr)	0.03	0.36	0.33	1.55	–	–	−0.2
2354	1,115	15	No	Gl(75), CrSp(tr), Olv(4), AlSp(1), Cpx(20), Opx(tr)	0.04	0.36	0.34	–	–	–	−0.3
2353	1,135	10.5	No	Gl(81), CrSp(tr), Olv(2), AlSp(1), Cpx(16), Opx(tr)	0.06	0.35	0.38	–	–	–	−0.3
2362	1,155	7.5	Yes	Gl(89), CrSp(1), Olv(1), Cpx(9)	0.02	0.32	0.35	–	–	–	−0.4
2351	1,185	8	No	Gl(99), CrSp(1)	0.13	–	–	–	–	–	−0.5
P = 700 MPa											
2370	950	96	Yes	Gl(12), Cpx(6), Opx(5), Pl(30), Hbl(45), Mt(2), Ilm(tr), V(6)	0.10	–	0.32	1.51	93.2	6.8	1.3
2376	975	96	Yes	Gl(17), Cpx(9), Opx(7), Pl(27), Hbl(39), Mt(1), V(1)	0.04	–	0.28	1.77	85.1	14.9	1.3
2387	1,000	96	Yes	Gl(20), Cpx(11), Opx(12), Pl(28), Hbl(27), Mt(2)	0.03	–	0.28	2.35	–	–	1.2
2388	1,025	96	Yes	Gl(36), Cpx(16), Opx(9), Pl(22), Hbl(14), Mt(3)	0.09	–	0.32	2.17	–	–	0.6
2374	1,050	72	Yes	Gl(51), Olv(7), Cpx(20), Opx(tr), Pl(20), Mt(2)	0.10	0.36	0.34	2.03	–	–	0.2
2379	1,100	15	Yes	Gl(79), CrSp(tr), Olv(3), Cpx(15), Pl(3)	0.03	0.32	0.30	1.60	–	–	−0.3
2369	1,150	8	Yes	Gl(99), CrSp(tr), Olv(1)	0.05	0.32	–	–	–	–	−0.5
2371	1,200	8	Yes	Gl(100)	–	–	–	–	–	–	−0.5
P = 400 MPa											
2381	975	96	Yes	Gl(17), Cpx(9), Opx(9), Pl(31), Hbl(32), Mt(2), V(5)	0.08	–	0.28	2.20	92.3	7.7	1.0
2390	1,000	96	Yes	Gl(20), Cpx(12), Opx(11), Pl(34), Hbl(19), Mt(4), V(3)	0.06	–	0.27	2.18	89.8	10.2	1.0
2380	1,025	72	Yes	Gl(52), Olv(5), Cpx(17), Pl(23), Mt(3)	0.06	0.32	0.31	2.20	–	–	0.3
2391	1,050	72	Yes	Gl(53), Olv(6), Cpx(14), Pl(25), Mt(2)	0.05	0.31	0.29	2.19	–	–	0.3
2389	1,075	15	Yes	Gl(77), CrSp(tr), Olv(6), Cpx(6), Pl(11)	0.06	0.29	0.31	1.73	–	–	−0.3
2384	1,125	10	Yes	Gl(98), CrSp(1), Olv(1)	0.20	0.30	–	–	–	–	−0.5

[a] AuPd capsules were pre-saturated with Fe: yes or no

[b] Phase abbreviations are: *Gl* glass, *CrSp* chromium spinel, *Olv* olivine, *AlSp* aluminum spinel, *Cpx* clinopyroxene, *Opx* orthopyroxene, *Pl* plagioclase, *Hbl* hornblende, *Mt* magnetite, *Ilm* ilmeno-hematite, *V* vapor. Modes (wt%) were calculated using least-squares regression for solid phases (XLFRAC; Stormer and Nicholls 1978), with Σr^2 indicating the quality of the regression. Fluid was estimated using Papale et al. (2006) as described in the text

[c] $K_D(Fe^{2+}–Mg)$ values were calculated as $(FeO_{sol} \times MgO_{liq})/(FeO_{liq} \times MgO_{sol})$

[d] $K_D(Ca–Na)$ values were calculated as $(CaO_{pl} \times Na_2O_{liq})/(CaO_{liq} \times Na_2O_{pl})$

[e] Wt% H_2O and CO_2 in the fluid phase was calculated using Papale et al. (2006)

[f] $\Delta ReReO_2$ is estimated by $2\log(XH_2O_{sv}/XH_2O_{bv})$, where XH_2O_{sv} is the mole fraction of H_2O in the real or fictive sample vapor and $XH2O_{bv}$ is the mole fraction of H_2O in the buffer vapor

EDS on the scanning electron microscope at the USGS in Menlo Park. Silicate samples and metal capsules were analyzed using the five-spectrometer JEOL JXA-8900 electron microprobe at the USGS in Menlo Park. Analytical conditions were optimized for each phase. Hydrous glass was analyzed with 15 kV accelerating potential, 2 nA beam current, and 10–20 μm spot size (depending on the size of glass pools), with Na and Al analyzed first in the routine, 20 s count times for Na and 30 s count times for all other elements. These conditions have been shown to minimize Na-loss and grow-in for Si and Al in hydrous glass and allow estimation of H_2O-by-difference (Morgan and London 1996). Instrumental conditions for crystalline phases were 15 kV accelerating potential, 20 nA (olivine and oxides), 15 nA (pyroxene and amphibole), and 5 nA (plagioclase), with a focused beam for all crystalline phases except plagioclase (5 μm spot size). Used and unused AuPd and Pt capsules were analyzed for Au, Pd, Fe, Pt, and Re with 25 kV accelerating potential, 20 nA beam current, and a focused beam. Standards were analyzed as unknowns throughout analytical sessions to monitor and correct for instrumental drift.

Results

Experimental conditions, phase assemblages, modes, and mineral–liquid exchange coefficients (K_Ds) are presented in Table 4. Average phase compositions with standard deviations and number of points averaged are reported in Table 5.

Approach to equilibrium

The experiments reported in this study are crystallization runs. Samples were first heated to near-liquidus temperatures, held for 30 min, and then set at the desired temperature for the duration of the run. This method eliminated relict phases and grew near-homogeneous phases in most runs. Preliminary runs (not reported) that were brought directly to P and T produced the same phase assemblages, but minerals were smaller and irregularly shaped, with more heterogeneous compositions. Equilibrium was facilitated by maintaining a constant bulk composition and fO_2 throughout the run by using Fe-saturated capsules and an appropriate amount of Re–ReO_2 buffer powder and mixed-volatile spike in the buffer assembly, and by maximizing the duration of each run, appropriate to the temperature conditions. A sufficient approach to equilibrium in these experiments is considered likely because (1) the glass is homogeneous and crystals are minimally zoned, with euhedral to subhedral habits (exceptions noted below), many reaching sizes of >100 μm (Fig. 2), (2) mass-balance calculations have sums of the squares of the residuals (Σr^2) less than 0.2 (Table 4), and (3) mineral–liquid element partitioning exchange K_Ds are consistent within each experiment and with values from the literature (Table 4). A few of the runs produced olivine with embayed or rounded shapes (Fig. 2b–d), similar to olivine grains produced by Draper and Johnston (1992) and Faure and Schiano (2005). We note no difference in the exchange K_Ds or quality of the mass-balance calculation for runs with non-euhedral olivine crystals, and we speculate that these grains attained their forms due to either surface energy or a reaction relation with other phases during synthesis. Olivine grains near their low-temperature stability limit have K_Ds somewhat higher (0.33–0.37) than the commonly referenced value of 0.3 for basaltic liquids (Roeder and Emslie 1970; Toplis 2005). Slightly elevated olivine–liquid exchange K_Ds have also been reported in other studies with evolved melts (Sisson et al. 2005, C. Till, written communication). The lowest-temperature runs produced crystal-rich assemblages with greater internal zoning and compositional variation between grains, as measured by higher standard deviations of their oxide components (Table 5).

Phase proportions

Phase proportions were calculated for each run using the multiple-regression least-squares approach (XLFRAC, Stormer and Nicholls 1978), which assumes that the weighted sum of all the crystalline phases and the quenched melt equals the starting composition (01SB872). In runs where the number of phases approaches the number of chemical components (highly crystalline, low-temperature runs), the modal abundances are not as reliably determined as for experiments with few phases. In order to assess the uncertainties of phase proportions, regressions were calculated using the average composition for each phase and also the average compositions plus and minus 1σ for each experiment. This yielded a total maximum variation of ~8 % in the crystallinity of each run, although samples with fewer than 20 % crystals had <5 % variation in crystallinity. This approach overestimates the uncertainties in modal proportions because many oxide components are not independently variable in minerals. Uncertainties for individual phase abundances vary between 2 and 20 % relative for phases with greater than 5 modal %. Phases with low modal abundances (<1 %) have the highest relative uncertainties (up to 50 %). Phases with less than 1 % modal abundance are reported as trace (tr), and phases with modes between 0.5 and 1 % are reported as 1 % (Table 4).

Table 5 Electron microprobe analyses of experimental phases

	Comp.	SiO_2	TiO_2	Al_2O_3	V_2O_3	Cr_2O_3	Fe_2O_3[a]	FeO[a]	MnO	MgO	CaO	NiO	Na_2O	K_2O	P_2O_5	Total	"H_2O[b]"
P = 900 MPa																	
Run 2364, 975°C																	
Glass[c] (25)[d]		60.7 (6)[e]	0.71 (6)	18.7 (3)	NA	NA	3.84	2.34 (21)	0.12 (5)	2.01 (13)	5.77 (12)	NA	3.64 (17)	1.43 (7)	0.73 (6)	93.9 (8)	6.1
Cpx (5)	$Wo_{39}En_{42}Fs_{19}$	49.0 (8)	0.70 (27)	6.40 (83)	NA	0.07 (1)		11.1 (1)	0.29 (3)	13.9 (3)	17.8 (5)	NA	0.67 (18)	0.04 (6)	NA	100.0 (2)	
Opx (4)	$Wo_{04}En_{68}Fs_{28}$	51.5 (8)	0.28 (4)	4.29 (89)	NA	0.04 (2)		17.7 (5)	0.39 (4)	23.9 (4)	1.84 (41)	NA	0.12 (10)	0.02 (2)	NA	100.0 (7)	
Pl (25)	$An_{50}Ab_{49}Or_{01}$	55.2 (4)	NA	27.5 (3)	NA	NA		0.68 (3)	NA	0.05 (1)	10.3 (2)	NA	5.50 (15)	0.17 (1)	NA	99.5 (5)	
Hbl (32)		41.0 (7)	2.38 (33)	15.2 (10)	NA	0.06 (3)		13.0 (3)	0.17 (3)	13.0 (5)	10.0 (4)	NA	2.65 (11)	0.29 (7)	NA	97.6 (5)	
Mt (4)		0.17 (7)	4.85 (5)	7.64 (9)	0.25 (1)	0.43 (5)	50.3	30.9 (5)	0.30 (1)	3.35 (4)	0.14 (2)	0.10 (3)	NA	NA	NA	98.5 (5)	
Run 2358, 995°C																	
Glass (23)		58.4 (6)	0.86 (9)	18.8 (2)	NA	NA	4.24	2.50 (36)	0.13 (5)	2.59 (27)	6.48 (32)	NA	4.06 (22)	1.36 (7)	0.59 (4)	94.5 (6)	5.5
Cpx (12)	$Wo_{42}En_{40}Fs_{18}$	48.2 (5)	0.67 (08)	6.50 (42)	NA	0.11 (12)		10.5 (3)	0.26 (2)	13.3 (3)	19.0 (6)	NA	0.63 (4)	0.01 (1)	NA	99.2 (4)	
Opx (8)	$Wo_{04}En_{67}Fs_{29}$	49.9(5)	0.29 (10)	6.37 (51)	NA	0.03 (4)		17.7 (9)	0.36 (1)	22.7 (9)	1.92 (40)	NA	0.08 (2)	0.01 (0)	NA	99.3 (2)	
Pl (35)	$An_{53}Ab_{46}Or_{01}$	54.8 (6)	NA	28.4 (4)	NA	NA		0.67 (3)	NA	0.07 (3)	10.8 (0)	NA	5.22 (23)	0.17 (2)	NA	100.1 (1)	
Hbl (28)		40.6 (3)	2.67 (23)	15.0 (4)	NA	0.08 (2)		12.7 (2)	0.18 (1)	13.0 (3)	10.1 (4)	NA	2.78 (5)	0.26 (3)	NA	97.3 (1)	
Mt (5)		0.20 (1)	5.02 (3)	8.76 (4)	0.26 (3)	0.18 (2)	50.0	30.8 (1)	0.30 (3)	3.92 (3)	0.17 (1)	0.10 (2)	NA	NA	NA	99.7 (2)	
Run 2360, 1015°C																	
Glass (20)		57.1 (5)	0.95 (5)	19.2 (2)	NA	NA	4.43	2.85 (9)	0.16 (6)	2.87 (7)	6.40 (8)	NA	4.25 (21)	1.24 (7)	0.56 (2)	94.9 (7)	5.1
Cpx (15)	$Wo_{41}En_{42}Fs_{17}$	47.7 (6)	0.75 (7)	7.25 (39)	NA	0.07 (2)		10.2 (4)	0.26 (3)	13.7 (3)	18.9 (6)	NA	0.67 (3)	0.00 (0)	NA	99.5 (9)	
Opx (5)	$Wo_{04}En_{68}Fs_{28}$	48.9 (3)	0.32 (4)	6.93 (64)	NA	0.06 (3)		17.6 (6)	0.32 (3)	24.0 (5)	1.70 (13)	NA	0.06 (1)	0.00 (0)	NA	99.9 (7)	
Pl (25)	$An_{55}Ab_{44}Or_{01}$	54.2 (3)	NA	29.0 (2)	NA	NA		0.69 (3)	NA	0.07 (1)	11.3 (2)	NA	5.04 (17)	0.14 (1)	NA	100.4 (2)	
Hbl (26)		39.5 (5)	2.81 (25)	15.8 (9)	NA	0.09 (3)		12.4 (3)	0.17 (2)	13.5 (3)	9.94 (44)	NA	2.91 (11)	0.29 (6)	NA	97.4 (7)	
Mt (22)		0.17 (2)	5.15 (11)	10.4 (2)	0.28 (3)	0.45 (18)	48.2	30.3 (4)	0.30 (1)	4.54 (8)	0.16 (3)	0.12 (2)	NA	NA	NA	100.0 (2)	
Run 2359, 1035°C																	
Glass (23)		54.3 (2)	1.16 (10)	19.6 (2)	NA	NA	4.67	3.63 (17)	0.16 (5)	3.78 (16)	7.07 (15)	NA	4.17 (13)	.98 (6)	0.52 (6)	96.4 (3)	3.6
Cpx (16)	$Wo_{41}En_{42}Fs_{17}$	48.2 (4)	0.80 (10)	7.32 (44)	NA	0.08 (2)		10.2 (4)	0.24 (3)	13.7 (5)	18.8 (6)	NA	0.68 (4)	0.01 (0)	NA	100.0 (4)	
Opx (17)	$Wo_{03}En_{71}Fs_{26}$	49.6 (9)	0.42 (7)	7.47 (115)	NA	0.08 (4)		15.8 (8)	0.29 (4)	24.6 (6)	1.63 (17)	NA	0.09 (2)	0.00 (1)	NA	100.0 (5)	
Pl (28)	$An_{58}Ab_{41}Or_{01}$	53.4 (6)	NA	29.4 (5)	NA	NA		0.68 (6)	NA	0.07 (0)	11.9 (4)	NA	4.70 (23)	0.13 (1)	NA	100.3 (2)	
Hbl (15)		40.4 (2)	3.03 (9)	15.3 (2)	NA	0.08 (3)		12.1 (2)	0.15 (1)	13.6 (1)	10.3 (2)	NA	2.94 (4)	0.34 (1)	NA	98.3 (2)	
Mt (26)		0.27 (11)	4.69 (13)	16.7 (6)	0.29 (2)	0.86 (16)	42.3	28.0 (9)	0.28 (2)	6.57 (18)	0.23 (4)	0.15 (3)	NA	NA	NA	100.4 (5)	
Run 2357, 1055 °C																	
Glass (24)		53.0 (5)	1.57 (6)	19.7 (2)	NA	NA	4.24	4.58 (13)	0.14 (4)	4.06 (12)	7.10 (13)	NA	4.34 (21)	0.92 (5)	0.35 (3)	97.1 (8)	2.9
AlSp (16)		0.15 (1)	0.71 (9)	51.3 (11)	0.09 (2)	0.21 (8)	15.1	18.0 (11)	0.17 (1)	14.7 (3)	0.14 (2)	0.22 (2)	NA	NA	NA	100.7 (3)	
Cpx (20)	$Wo_{42}En_{42}Fs_{16}$	47.1 (2)	1.21 (5)	9.48 (34)	NA	0.09 (1)		8.90 (18)	0.20 (1)	13.3 (1)	18.7 (5)	NA	0.75 (3)	0.01 (0)	NA	99.7 (7)	
Opx (15)	$Wo_{04}En_{73}Fs_{23}$	49.4 (7)	0.47 (5)	8.97 (86)	NA	0.10 (1)		13.7 (2)	0.24 (1)	24.8 (5)	1.71 (6)	NA	0.09 (1)	0.00 (0)	NA	99.4 (5)	
Pl (25)	$An_{58}Ab_{41}Or_{01}$	53.3 (0)	NA	29.3 (3)	NA	NA		0.70 (2)	NA	0.10 (2)	12.0 (1)	NA	4.60 (5)	0.13 (1)	NA	100.1 (3)	

Table 5 continued

	Comp.	SiO_2	TiO_2	Al_2O_3	V_2O_3	Cr_2O_3	Fe_2O_3[a]	FeO[a]	MnO	MgO	CaO	NiO	Na_2O	K_2O	P_2O_5	Total	"H_2O[b]"
Run 2356, 1075°C																	
Glass (19)		51.5 (5)	1.41 (7)	20.0 (2)	NA	NA	4.28	4.88 (10)	0.15 (4)	4.72 (7)	7.81 (13)	NA	4.16 (21)	0.77 (5)	0.29 (2)	97.2 (7)	2.8
AlSp (5)		0.12 (1)	0.39 (2)	58.6 (6)	0.08 (1)	0.52 (4)	7.85	16.2 (3)	0.13 (3)	16.5 (1)	0.07 (1)	0.20 (3)	NA	NA	NA	100.8 (4)	
Cpx (20)	$Wo_{41}En_{45}Fs_{14}$	48.1 (4)	1.03 (8)	9.28 (21)	NA	0.12 (1)		8.23 (24)	0.20 (3)	14.4 (4)	18.1 (5)	NA	0.65 (2)	0.00 (0)	NA	100.1 (4)	
Opx (20)	$Wo_{03}En_{76}Fs_{21}$	50.4 (6)	0.39 (1)	8.33 (59)	NA	0.10 (2)		12.6 (1)	0.23 (1)	26.1 (4)	1.57 (5)	NA	0.07 (1)	0.00 (0)	NA	99.8 (5)	
Pl (25)	$An_{62}Ab_{37}Or_{01}$	52.2 (3)	NA	30.1 (1)	NA	NA		0.57 (4)	NA	0.09 (1)	12.67 (7)	NA	4.20 (4)	0.10 (1)	NA	99.9 (1)	
Run 2363, 1095°C																	
Glass (25)		50.6 (6)	1.34 (9)	19.7 (2)	NA	NA	4.25	5.21 (21)	0.16 (5)	5.41 (11)	8.25 (12)	NA	3.99 (17)	0.69 (5)	0.37 (1)	97.7 (5)	2.3
CrSp (4)	cores	0.07 (2)	0.60 (8)	29.5 (5)	0.15 (1)	21.6 (2)	17.7	19.4 (7)	0.24 (3)	11.4 (1)	0.11 (2)	0.18 (2)	NA	NA	NA	101.0 (7)	
Olv (30)	Fo_{79}	38.3 (3)	NA	NA	NA	NA		18.9 (4)	0.23 (3)	41.8 (4)	0.25 (2)	0.14 (1)	NA	NA	NA	99.5 (4)	
AlSp (4)		0.13 (2)	0.38 (3)	57.3 (9)	0.10 (4)	2.01 (74)	8.57	14.5 (6)	0.15 (2)	17.6 (4)	0.11 (1)	0.18 (4)	NA	NA	NA	101.0 (5)	
Cpx (15)	$Wo_{41}En_{45}Fs_{14}$	48.0 (5)	0.94 (7)	9.07 (61)	NA	0.19 (7)		8.18 (14)	0.20 (0)	14.5 (6)	18.1 (1)	NA	0.61 (2)	0.01 (0)	NA	99.8 (1)	
Opx (15)	$Wo_{03}En_{77}Fs_{20}$	50.4 (1)	0.36 (1)	8.30 (20)	NA	0.07 (3)		12.6 (1)	0.22 (2)	26.8 (3)	1.55 (3)	NA	0.06 (1)	0.00 (0)	NA	100.3 (3)	
Pl (25)	$An_{64}Ab_{35}Or_{01}$	51.4 (5)	NA	30.5 (3)	NA	NA		0.57 (4)	NA	0.10 (2)	13.0 (1)	NA	4.01 (13)	0.08 (1)	NA	99.5 (6)	
Run 2354, 1115°C																	
Glass (16)		50.6 (5)	1.34 (7)	19.5 (4)	NA	NA	4.00	5.20 (10)	0.12 (3)	5.89 (8)	8.59 (16)	NA	3.85 (15)	0.67 (6)	0.24 (3)	97.0 (7)	3.0
CrSp (5)	cores	0.13 (1)	2.48 (4)	12.6 (2)	0.22 (2)	19.52 (19)	32.4	24.6 (3)	0.31 (3)	6.93 (9)	0.11 (2)	0.11 (1)	NA	NA	NA	99.4 (5)	
Olv (20)	Fo_{81}	38.6 (1)	NA	NA	NA	NA		17.5 (0)	0.23 (0)	43.0 (0)	0.22 (1)	0.16 (1)	NA	NA	NA	99.7 (1)	
AlSp (9)		0.13 (1)	0.32 (2)	60.9 (3)	0.09 (1)	0.59 (13)	5.79	14.9 (3)	0.12 (2)	17.6 (2)	0.12 (2)	0.17 (2)	NA	NA	NA	100.7 (3)	
Cpx (15)	$Wo_{41}En_{46}Fs_{13}$	48.6 (6)	0.89 (12)	9.06 (61)	NA	0.11 (04)		7.61 (29)	0.20 (0)	14.8 (2)	18.3 (5)	NA	0.59 (1)	0.00 (0)	NA	100.2 (4)	
Opx (15)	$Wo_{04}En_{78}Fs_{18}$	52.0 (8)	0.31 (5)	6.75 (93)	NA	0.12 (12)		11.3 (6)	0.24 (2)	27.3 (6)	1.80 (20)	NA	0.07 (0)	0.00 (0)	NA	99.8 (1)	
Run 2353, 1135°C																	
Glass (15)		50.5 (4)	1.34 (7)	18.8 (3)	NA	NA	4.05	5.53 (14)	0.13 (4)	6.28 (10)	8.79 (13)	NA	3.69 (15)	0.63 (4)	0.20 (2)	97.8 (8)	2.2
CrSp (5)		0.09 (1)	0.66 (2)	26.0 (1)	0.16 (2)	22.9 (1)	20.0	17.1 (1)	0.25 (2)	12.3 (1)	0.17 (1)	0.18 (2)	NA	NA	NA	99.8 (1)	
Olv (15)	Fo_{81}	38.5 (1)	NA	NA	NA	NA		17.0 (4)	0.28 (1)	42.8 (3)	0.27 (1)	0.17 (0)	NA	NA	NA	99.0 (1)	
AlSp (4)		0.19 (2)	0.48(4)	49.3 (31)	0.09(2)	3.12 (277)	16.1	14.4 (8)	0.14 (1)	16.7 (5)	0.15 (3)	0.30 (2)	NA	NA	NA	101.1 (1)	
Cpx (15)	$Wo_{39}En_{47}Fs_{14}$	47.8 (3)	0.86 (9)	9.30 (57)	NA	0.10 (3)		8.19 (19)	0.17 (2)	14.9 (4)	17.9 (3)	NA	0.63 (2)	0.01 (1)	NA	99.9 (3)	
Opx (15)	$Wo_{04}En_{79}Fs_{17}$	51.1 (1)	0.30 (1)	8.14 (29)	NA	0.07 (4)		10.8 (1)	0.24 (1)	27.5 (1)	1.84 (12)	NA	0.08 (1)	0.00 (0)	NA	100.1 (3)	
Run 2362, 1155°C																	
Glass (20)		50.4 (3)	1.23 (9)	17.9 (3)	NA	NA	3.96	5.67 (13)	0.13 (6)	7.40 (13)	9.44 (13)	NA	3.09 (15)	0.52 (5)	0.21 (3)	98.2 (5)	1.8
CrSp (3)[f]		1.03 (28)	2.66 (5)	21.5 (4)	0.24 (2)	20.8 (3)	20.0	19.0 (1)	0.20 (0)	12.1 (1)	0.36 (2)	0.23 (1)	NA	NA	NA	98.2 (3)	
Olv (35)	Fo_{84}	39.4 (2)	NA	NA	NA	NA		14.4 (8)	0.20 (2)	45.5 (5)	0.25 (1)	0.22 (4)	NA	NA	NA	99.9 (3)	
Cpx (40)	$Wo_{37}En_{51}Fs_{12}$	48.9 (4)	0.65 (7)	8.10 (62)	NA	0.35 (11)		7.33 (29)	0.17 (2)	16.7 (3)	17.0 (6)	NA	0.61 (4)	0.01 (1)	NA	99.9 (2)	

Table 5 continued

Comp.		SiO_2	TiO_2	Al_2O_3	V_2O_3	Cr_2O_3	Fe_2O_3[a]	FeO[a]	MnO	MgO	CaO	NiO	Na_2O	K_2O	P_2O_5	Total	"H_2O[b]"
Run 2351, 1185°C																	
Glass (18)		50.2 (3)	1.18 (6)	17.1 (2)	NA	NA	3.80	5.55 (10)	0.17 (3)	8.24 (9)	10.1 (1)	NA	3.07 (13)	0.52 (6)	0.17 (4)	97.9 (5)	2.1
CrSp (3)		0.15 (2)	1.6 (9)	23.7 (13)	0.15 (0)	21.1 (2)	22.7	15.6 (17)	0.22 (1)	13.5 (4)	0.14 (4)	0.18 (1)	NA	NA	NA	99.0 (4)	
P = 700 MPa																	
Run 2370, 950°C																	
Glass (24)		65.2 (6)	0.73 (8)	17.4 (5)	NA	NA	2.36	1.42 (36)	0.11 (4)	1.92 (39)	4.70 (21)	NA	3.63 (45)	1.96 (9)	0.55 (6)	94.3 (6)	5.7
Cpx (8)	$Wo_{41}En_{44}Fs_{15}$	49.7 (6)	0.71 (15)	5.12 (90)	NA	0.04 (2)		8.91 (40)	0.29 (1)	15.1 (5)	19.4 (7)	NA	0.53 (5)	0.02 (2)	NA	99.8 (5)	
Opx (7)	$Wo_{03}En_{76}Fs_{21}$	52.8 (4)	0.29 (7)	3.96 (48)	NA	0.03 (1)		13.5 (5)	0.45 (3)	27.7 (9)	1.73 (48)	NA	0.07 (4)	0.02(3)	NA	100.6 (5)	
Pl (25)	$An_{51}Ab_{48}Or_{01}$	55.6 (9)	NA	27.9 (6)	NA	NA		0.85 (3)	NA	0.10 (5)	10.5 (6)	NA	5.35 (33)	0.18 (2)	NA	100.4 (2)	
Hbl (38)		41.8 (11)	2.17 (37)	13.9 (14)	NA	0.06 (2)		11.9 (8)	0.19 (3)	14.3 (9)	10.6 (5)	NA	2.47 (15)	0.27 (6)	NA	97.7 (3)	
Mt (3)		0.34 (3)	3.69 (6)	5.14 (6)	0.20 (1)	0.16 (5)	57.3	28.3 (5)	0.40 (1)	4.44 (15)	0.25 (9)	0.14 (2)	NA	NA	NA	100.4 (3)	
Ilm (6)		0.18 (7)	20.5 (5)	1.35 (1)	0.24 (1)	0.09 (1)	60.0	14.1 (1)	0.12 (1)	2.32 (4)	0.25 (9)	0.03 (1)	NA	NA	NA	99.1 (6)	
Run 2376, 975°C																	
Glass (19)		61.8 (8)	0.74 (8)	18.7 (3)	NA	NA	3.07	2.06 (20)	0.13 (10)	2.10 (15)	5.41 (19)	NA	3.91 (34)	1.43 (4)	0.67 (5)	94.6 (8)	5.4
Cpx (2)	$Wo_{40}En_{44}Fs_{16}$	49.9 (1)	0.54 (7)	4.76 (21)	NA	0.01 (1)		9.63 (66)	0.32 (5)	14.8 (2)	19.1 (4)	NA	0.51 (1)	0.05 (3)	NA	99.6 (3)	
Opx (6)	$Wo_{03}En_{71}Fs_{26}$	51.2 (6)	0.25 (3)	4.47 (52)	NA	0.01 (2)		16.4 (3)	0.42 (5)	25.4 (6)	1.65 (31)	NA	0.06 (2)	0.05 (1)	NA	99.9 (5)	
Pl (21)	$An_{57}Ab_{42}Or_{01}$	53.9 (12)	NA	28.7 (6)	NA	NA		0.74 (12)	NA	0.14 (10)	11.8 (8)	NA	4.82 (49)	0.15 (3)	NA	100.2 (7)	
Hbl (22)		41.1 (5)	2.39 (32)	14.7 (10)	NA	0.08 (4)		12.2 (5)	0.19 (3)	13.8 (5)	10.3 (1)	NA	2.69 (9)	0.29 (8)	NA	97.6 (9)	
Mt (22)		0.12 (2)	4.79 (8)	6.32 (9)	0.24 (3)	0.22 (6)	53.9	30.2 (4)	0.35 (4)	3.93 (6)	0.15 (4)	0.08 (3)	NA	NA	NA	100.2 (5)	
Run 2387, 1000°C																	
Glass (20)		58.8 (5)	0.82 (7)	18.7 (4)	NA	NA	3.72	2.44 (18)	0.17 (5)	2.67 (10)	5.80 (18)	NA	4.79 (21)	1.42 (6)	0.68 (6)	95.6 (6)	4.4
Cpx (11)	$Wo_{41}En_{44}Fs_{15}$	49.0 (4)	0.78 (8)	5.56 (40)	NA	0.04 (2)		8.96 (30)	0.27 (2)	14.9 (3)	19.3 (4)	NA	0.55 (4)	0.01 (1)	NA	99.3 (2)	
Opx (8)	$Wo_{04}En_{73}Fs_{23}$	51.3 (7)	0.40 (7)	4.95 (96)	NA	0.06 (2)		14.7 (8)	0.35 (4)	25.9 (5)	1.86 (18)	NA	0.07 (20)	0.01 (1)	NA	99.6 (3)	
Pl (26)	$An_{60}Ab_{39}Or_{01}$	52.7 (4)	NA	29.5 (5)	NA	NA		0.77 (8)	NA	0.10 (5)	12.5 (4)	NA	4.41 (22)	0.12 (2)	NA	100.1 (6)	
Hbl (26)		40.6 (3)	3.04 (25)	14.5 (4)	NA	0.08 (3)		11.6 (2)	0.15 (3)	13.9 (3)	10.7 (3)	NA	2.91 (8)	0.34 (4)	NA	97.7 (5)	
Mt (2)		0.19 (2)	5.00 (5)	7.37 (13)	0.29 (3)	0.39 (13)	51.9	29.5 (1)	0.38 (3)	4.4 (1)	0.24 (5)	0.23 (5)	NA	NA	NA	99.9 (2)	
Run 2388, 1025°C																	
Glass (19)		55.7 (3)	1.13 (09)	19.3 (2)	NA	NA	4.05	3.38 (19)	0.15 (6)	3.67 (22)	6.67 (26)	NA	4.48 (17)	1.03 (7)	0.43 (5)	96.7 (4)	3.3
Cpx (13)	$Wo_{41}En_{43}Fs_{15}$	48.2 (5)	1.16 (9)	7.00 (58)	NA	0.08 (4)		8.86 (22)	0.22 (2)	14.4 (3)	19.3 (4)	NA	0.60 (3)	0.01 (1)	NA	99.8 (3)	
Opx (10)	$Wo_{03}En_{75}Fs_{22}$	50.9 (4)	0.41 (5)	6.09 (51)	NA	0.05 (3)		13.6 (4)	0.32 (3)	26.6 (5)	1.58 (20)	NA	0.07 (3)	0.01 (1)	NA	99.6 (4)	
Pl (13)	$An_{64}Ab_{35}Or_{01}$	51.4 (7)	NA	29.9 (5)	NA	NA		0.70 (7)	NA	0.10 (1)	13.1 (3)	NA	4.07 (20)	0.09 (2)	NA	99.4 (6)	
Hbl (14)		40.3 (4)	3.38 (14)	14.6 (4)	NA	0.06 (2)		10.8 (2)	0.15 (2)	14.2 (1)	10.9 (1)	NA	2.92 (6)	0.32 (2)	NA	97.7 (3)	
Mt (20)		0.16 (4)	5.27 (6)	11.1 (2)	0.25 (2)	0.47 (14)	48.4	28.3 (3)	0.33 (2)	6.08 (6)	0.17 (4)	0.15 (3)	NA	NA	NA	100.6 (3)	

Table 5 continued

	Comp.	SiO_2	TiO_2	Al_2O_3	V_2O_3	Cr_2O_3	Fe_2O_3[a]	FeO[a]	MnO	MgO	CaO	NiO	Na_2O	K_2O	P_2O_5	Total	"H_2O[b]"
Run 2374, 1050°C																	
Glass (23)		52.2 (4)	1.53 (13)	19.7 (2)	NA	NA	4.36	4.38 (16)	0.14 (8)	4.57 (10)	7.34 (15)	NA	4.47 (14)	0.90 (4)	0.40 (6)	97.0 (7)	3.0
Olv (30)	Fo_{79}	38.5 (1)	NA	NA	NA	NA		19.3 (5)	0.31 (2)	41.6 (5)	0.19 (1)	0.13 (3)	NA	NA	NA	100.0 (5)	
Cpx (30)	$Wo_{42}En_{43}Fs_{15}$	47.8 (6)	1.25 (11)	7.62 (59)	NA	0.10 (6)		8.83 (26)	0.20 (3)	14.3 (4)	19.2 (4)	NA	0.58 (3)	0.00 (0)	NA	99.9 (8)	
Opx (18)	$Wo_{03}En_{76}Fs_{21}$	50.5 (7)	0.45 (4)	6.51 (86)	NA	0.07 (5)		13.4 (4)	0.29 (4)	27.0 (8)	1.56 (28)	NA	0.06 (2)	0.00 (0)	NA	99.9 (10)	
Pl (28)	$An_{64}Ab_{35}Or_{01}$	51.7 (7)	NA	30.1 (4)	NA	NA		0.67 (9)	NA	0.10 (2)	13.4 (4)	NA	4.00 (21)	0.10 (2)	NA	100.0 (8)	
Mt (30)		0.14 (1)	6.00 (8)	15.2 (1)	0.22 (3)	0.59 (9)	43.2	27.7 (5)	0.26 (2)	7.44 (6)	0.17 (2)	0.14 (1)	NA	NA	NA	101.0 (6)	
Run 2379, 1100°C																	
Glass (17)		50.6 (5)	1.37 (10)	19.4 (25)	NA	NA	3.98	5.78 (20)	0.17 (8)	5.50 (16)	8.63 (19)	NA	3.66 (18)	0.64 (4)	0.30 (4)	98.4 (7)	1.6
CrSp (3)		0.09 (4)	1.63 (86)	19.1 (5)	0.20 (1)	20.08 (103)	27.6	23.2 (2)	0.31 (0)	8.31 (33)	0.17 (6)	0.15 (3)	NA	NA	NA	100.9 (9)	
Olv (25)	Fo_{80}	38.8 (0)	NA	NA	NA	NA		18.2 (6)	0.27 (1)	42.2 (5)	0.27 (4)	0.11 (1)	NA	NA	NA	99.8 (3)	
Cpx (27)	$Wo_{42}En_{45}Fs_{13}$	47.7 (5)	0.98 (11)	8.45 (46)	0.29 (7)	NA		7.56 (47)	0.18 (3)	14.7 (4)	19.4 (6)	NA	0.50 (5)	0.00 (0)	NA	99.7 (7)	
Pl (18)	$An_{67}Ab_{32}Or_{01}$	51.7 (3)	NA	30.2 (3)	NA	NA		0.63 (9)	NA	0.14 (3)	13.9 (2)	NA	3.69 (17)	0.09 (2)	NA	100.3 (5)	
Run 2369, 1150°C																	
Glass (20)		49.6 (5)	1.27 (6)	17.4 (2)	NA	NA	3.83	5.89 (10)	0.14 (5)	7.84 (8)	10.2 (1)	NA	3.07 (13)	0.48 (5)	0.31 (3)	97.5 (6)	2.5
CrSp (4)		0.24 (16)	0.66 (1)	36.7 (2)	0.12 (1)	22.5 (1)	9.92	14.8 (1)	0.19 (1)	15.4 (1)	0.19 (1)	0.08 (0)	NA	NA	NA	100.7 (2)	
Olv (23)	Fo_{85}	39.4 (2)	NA	NA	NA	NA		13.9 (2)	0.19 (1)	46.1 (2)	0.24 (2)	0.09 (3)	NA	NA	NA	99.9 (5)	
Run 2371, 1200°C																	
Glass (26)		50.2 (4)	1.18 (9)	17.0 (4)	NA	NA	3.75	5.89 (17)	0.15 (5)	8.24 (14)	10.1 (1)	NA	2.91 (21)	0.48 (3)	0.18 (4)	98.2 (6)	1.8
P = 400 MPa																	
Run 2381, 975°C																	
Glass (20)		61.4 (6)	0.97 (7)	18.1 (6)	NA	NA	2.70	2.12 (9)	0.13 (4)	2.51 (13)	5.39 (13)	NA	4.41 (13)	1.48 (6)	0.71 (9)	96.0 (4)	4.0
Cpx (9)	$Wo_{41}En_{46}Fs_{13}$	50.6 (4)	0.56 (7)	3.89 (7)	NA	0.03 (2)		8.13 (46)	0.30 (5)	15.7 (3)	19.6 (7)	NA	0.42 (4)	0.01 (1)	NA	99.2 (7)	
Opx (8)	$Wo_{04}En_{74}Fs_{22}$	53.3 (5)	0.24 (5)	2.94 (98)	NA	0.03 (2)		14.2 (8)	0.43 (3)	27.3 (8)	1.84 (40)	NA	0.05 (3)	0.01 (1)	NA	100.2 (7)	
Pl (19)	$An_{59}Ab_{40}Or_{01}$	53.2 (5)	NA	29.1 (4)	NA	NA		0.88 (7)	NA	0.12 (3)	12.2 (4)	NA	4.55 (22)	0.14 (3)	NA	100.3 (4)	
Hbl (25)		40.6 (6)	2.64 (33)	14.7 (7)	NA	NA		11.9 (5)	0.17 (3)	13.8 (4)	10.4 (3)	NA	2.89 (10)	0.23 (5)	NA	97.5 (6)	
Mt (26)		0.16 (4)	4.70 (7)	5.67 (7)	0.22 (3)	0.21 (6)	55.4	27.1 (5)	0.41 (2)	5.62 (7)	0.20 (5)	0.14 (2)	NA	NA	NA	99.9 (6)	
Run 2390, 1000°C																	
Glass (20)		58.5 (3)	1.10 (13)	18.5 (2)	NA	NA	3.30	2.67 (16)	0.16 (6)	3.08 (8)	6.09 (14)	NA	4.67 (18)	1.33 (8)	0.59 (8)	96.0 (5)	4.0
Cpx (2)	$Wo_{41}En_{46}Fs_{13}$	50.1 (2)	0.77 (12)	4.31 (6)	NA	NA		7.79 (50)	0.30 (0)	15.8 (5)	19.7 (9)	NA	0.47 (7)	0.02 (2)	NA	99.3 (1)	
Opx (5)	$Wo_{05}En_{76}Fs_{19}$	52.0 (10)	0.49 (21)	4.48 (120)	NA	NA		11.8 (7)	0.37 (5)	26.7 (15)	2.20 (91)	NA	0.30 (29)	0.05 (6)	NA	98.4 (7)	
Pl (17)	$An_{60}Ab_{39}Or_{01}$	52.4 (5)	NA	29.4 (5)	NA	NA		0.89 (11)	NA	0.14 (4)	12.7 (4)	NA	4.45 (25)	0.11 (2)	NA	100.0 (6)	
Hbl (16)		40.4 (6)	3.27 (22)	14.7 (6)	NA	NA		10.8 (3)	0.16 (2)	14.1 (3)	10.6 (3)	NA	3.01 (8)	0.26 (5)	NA	97.3 (3)	
Mt (15)		0.12 (4)	5.36 (13)	6.77 (7)	0.23 (4)	0.26 (6)	53.5	27.7 (7)	0.39 (2)	5.92 (4)	0.18 (4)	0.11 (3)	NA	NA	NA	100.5 (6)	

Table 5 continued

	Comp.	SiO_2	TiO_2	Al_2O_3	V_2O_3	Cr_2O_3	Fe_2O_3[a]	FeO[a]	MnO	MgO	CaO	NiO	Na_2O	K_2O	P_2O_5	Total	"H_2O"[b]
Run 2380, 1025°C																	
Glass (22)		54.3 (5)	1.48 (27)	18.5 (2)	NA	NA	4.27	4.30 (26)	0.18 (7)	4.23 (12)	7.26 (18)	NA	4.27 (21)	0.89 (5)	0.41 (6)	96.7 (7)	3.3
Olv (27)	Fo_{80}	38.5 (2)	NA	NA	NA	NA		18.6 (4)	0.34 (10)	42.3 (3)	0.23 (12)	0.10 (5)	NA	NA	NA	100.1 (5)	
Cpx (27)	$Wo_{43}En_{43}Fs_{14}$	48.2 (5)	1.27 (15)	6.13 (54)	NA	0.11 (4)		8.62 (35)	0.22 (2)	14.5 (4)	20.1 (6)	NA	0.48 (5)	0.01 (1)	NA	99.6 (4)	
Pl (25)	$An_{67}Ab_{32}Or_{01}$	51.3 (4)	NA	30.5 (3)	NA	NA		0.90 (8)	NA	0.13 (5)	13.7 (3)	NA	3.67 (15)	0.09 (2)	NA	100.3 (3)	
Mt (32)		0.24 (6)	6.67 (13)	9.94 (21)	0.31 (2)	0.98 (19)	45.9	28.5 (6)	0.32 (3)	6.49 (7)	0.24 (7)	0.12 (2)	NA	NA	NA	99.7 (5)	
Run 2391, 1050°C																	
Glass (18)		53.7 (3)	1.71 (4)	18.0 (1)	NA	NA	4.51	4.46 (21)	0.18 (7)	4.33 (6)	7.87 (14)	NA	4.13 (16)	0.86 (6)	0.31 (7)	97.1 (4)	2.9
Olv (32)	Fo_{80}	38.7 (4)	NA	NA	NA	NA		18.1 (2)	0.35 (2)	42.5 (3)	0.22 (2)	0.08 (2)	NA	NA	NA	99.9 (5)	
Cpx (18)	$Wo_{43}En_{43}Fs_{14}$	48.4 (4)	1.11 (7)	5.93 (40)	NA	0.08 (4)		8.21 (20)	0.21 (2)	14.6 (4)	20.0 (4)	NA	0.49 (10)	0.02 (2)	NA	99.1 (5)	
Pl (17)	$An_{67}Ab_{32}Or_{01}$	50.9 (6)	NA	30.6 (3)	NA	NA		0.92 (9)	NA	0.14 (3)	13.9 (3)	NA	3.71 (22)	0.09 (1)	NA	100.1 (5)	
Mt (7)		0.18 (5)	6.47 (18)	8.41 (17)	0.29 (3)	0.74 (19)	49.3	28.8 (5)	0.32 (1)	6.32 (12)	0.19 (4)	0.08 (5)	NA	NA	NA	101.1 (4)	
Run 2389, 1075°C																	
Glass (23)		50.4 (5)	1.46 (12)	18.0 (2)	NA	NA	4.41	5.87 (24)	0.17 (5)	5.45 (15)	9.65 (16)	NA	3.52 (20)	0.62 (4)	0.31 (4)	97.8 (6)	2.2
CrSp (3)		0.34 (27)	1.74 (41)	20.1 (20)	0.30 (1)	19.9 (13)	26.0	21.8 (5)	0.30 (1)	9.41 (20)	0.20 (5)	0.16 (1)	NA	NA	NA	100.2 (4)	
Olv (24)	Fo_{81}	38.6 (2)	NA	NA	NA	NA		17.3 (3)	0.26 (1)	43.4 (2)	0.26 (1)	0.12 (2)	NA	NA	NA	99.9 (4)	
Cpx (20)	$Wo_{45}En_{42}Fs_{13}$	47.8 (4)	1.14 (14)	7.17 (41)	NA	0.31 (7)		7.68 (27)	0.16 (1)	14.0 (1)	20.7 (3)	NA	0.42 (3)	0.00 (0)	NA	99.4 (3)	
Pl (16)	$An_{72}Ab_{28}Or_{00}$	50.1 (3)	NA	31.2 (3)	NA	NA		0.87 (10)	NA	0.15 (1)	14.8 (2)	NA	3.14 (12)	0.07 (2)	NA	100.3 (4)	
Run 2384, 1125°C																	
Glass (23)		50.5 (4)	1.23 (10)	17.3 (2)	NA	NA	3.70	5.75 (15)	0.16 (3)	7.61 (14)	10.1 (2)	NA	2.87 (11)	0.45 (4)	0.35 (5)	98.2 (6)	1.8
CrSp (5)		0.15 (6)	0.75 (9)	29.3 (2)	0.14 (2)	22.8 (2)	17.1	15.9 (5)	0.21 (2)	13.7 (1)	0.18 (2)	0.16 (4)	NA	NA	NA	100.4 (5)	
Olv (22)	Fo_{86}	39.40 (3)	NA	NA	NA	NA		13.3 (2)	0.21 (2)	46.5 (3)	0.25 (3)	0.16 (2)	NA	NA	NA	99.8 (5)	

Olv olivine, *Cpx* clinopyroxene, *CrSp* chromium spinel, *AlSp* aluminum spinel, *Opx* orthopyroxene, *Pl* plagioclase, *Hbl* hornblende, *Mt* magnetite, *Ilm* ilmeno-hematite. NA indicates not analyzed

[a] Fe_2O_3 and FeO calculated for glass using experimental conditions and the expression of Kress and Carmichael (1991). Fe_2O_3 and FeO calculated for spinels assuming a 3 cation–4 oxygen stoichiometry. Analytical error was not propagated in the Fe_2O_3 calculations

[b] "H_2O" was calculated by difference between 100 % and the glass total, including Fe_2O_3

[c] Glass analyses normalized to 100 % anhydrous after Fe_2O_3 was calculated. Original unnormalized total is reported

[d] Number of probe analyses

[e] One standard deviation of replicate analyses in terms of least cited units

[f] Cr-spinel grains in this sample were <3 microns; therefore, the beam also excited some of the surrounding glass, hence the high SiO_2 and CaO concentrations

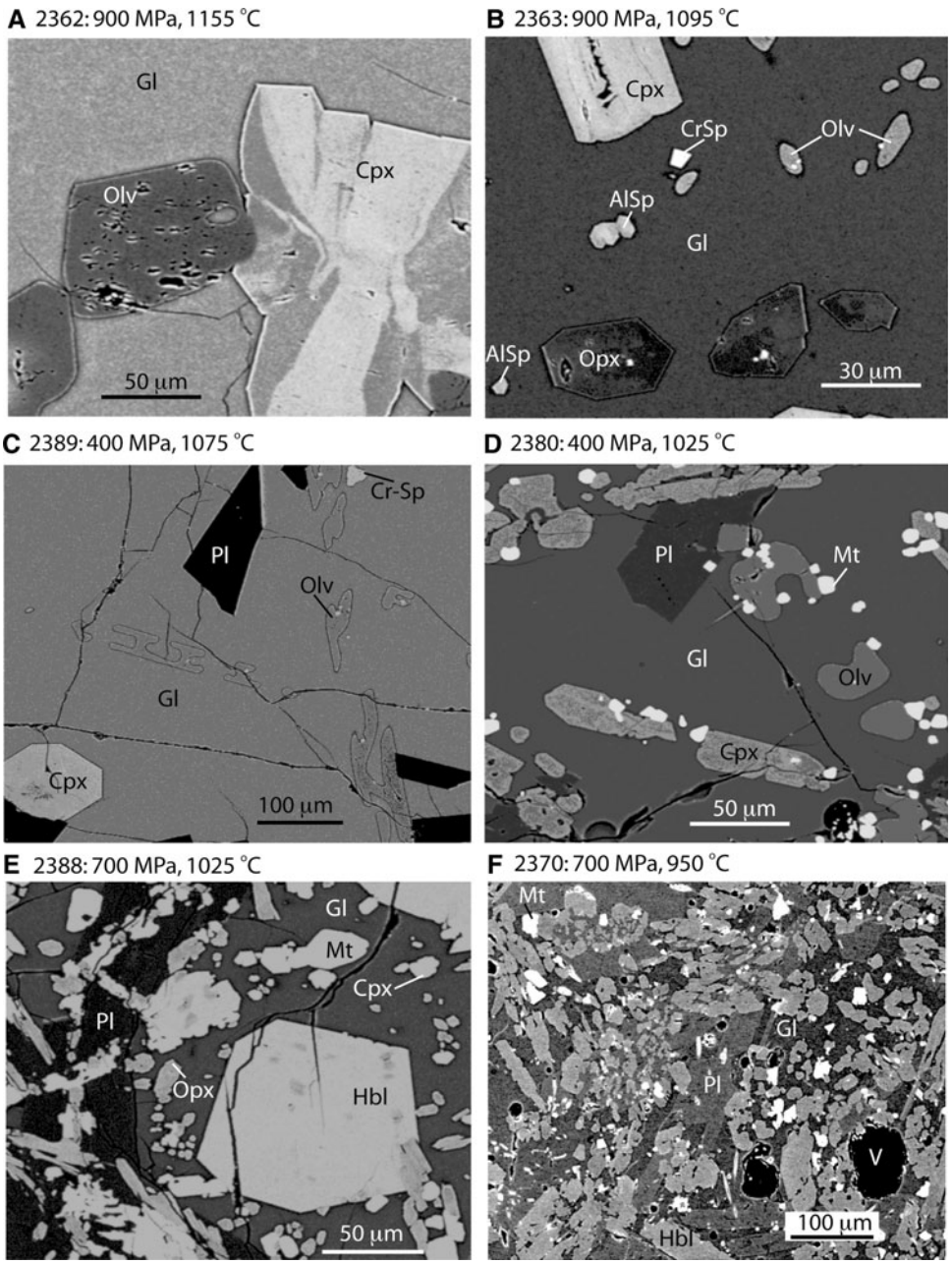

Fig. 2 Back-scattered electron images of selected run products. Each image is labeled with run number, pressure, and temperature. Scale bars are in microns. Phase abbreviations: *Gl* glass, *Olv* olivine, *Cpx* clinopyroxene, *CrSp* chromium spinel, *AlSp* aluminum spinel, *Opx* orthopyroxene, *Pl* plagioclase, *Mt* magnetite, *Hbl* hornblende, and *V* vapor

Oxidation states

Melt H_2O concentrations have been analyzed by FTIR (Tables 2, 3), can be estimated from electron-probe summation deficits (Table 5), and also from mass-balance phase proportions, assuming that H_2O is conserved in melt, amphibole, and vapor and that amphibole has H_2O similar to natural igneous hornblendes ($\sim$1.75 wt%: Dodge et al. 1968). Melt CO_2 concentrations were not measured but can be estimated by assuming that CO_2 is conserved only in melt and vapor. Deviations of runs from the Re–ReO_2 buffer (Pownceby and O'Neill 1994) can then be estimated (Sisson et al. 2005) using $(XH_2O_{sv}/XH_2O_{bv})^2$, where XH_2O_{sv} is the mole fraction of H_2O in a real or fictive H_2O–CO_2 vapor that would saturate the sample at its H_2O concentration, estimated from Papale et al. (2006), and XH_2O_{bv} is the mole fraction H_2O in the buffer vapor. These estimates indicate that the fO_2s of near-liquidus runs were slightly low relative to the buffer ($\Delta ReReO_2 = -0.5$) (due to the lower-than-intended bulk H_2O concentration), matched the buffer at melt fractions around 50–60 wt%, and rose above the buffer with further crystallization (to $\Delta ReReO_2 = +1.3$ at <20 wt% melt) (Table 4).

Phase stabilities

Figure 3 shows phase stability fields for basalt 01SB872 with 2 wt% H_2O, 650 ppm CO_2, at close to Re–ReO_2 with experiments plotted at 900, 700, and 400 MPa. The 0.1 MPa phase stabilities were estimated using MELTS at Re–ReO_2 (Ghiorso and Sack 1995; Asimow and Ghiorso 1998). The stability field for the H_2O–CO_2 vapor was estimated using Papale et al. (2006), as described following. At pressures less than 200 MPa, vapor is predicted to be the liquidus phase, whereas Cr-spinel is the liquidus phase at pressures above 200 MPa. Cr-spinel is predicted to crystallize at ~1,250 °C at 0.1 MPa (MELTS, Ghiorso and Sack 1995; Asimow and Ghiorso 1998) and estimated at ~1,190 °C at 900 MPa. At 900 MPa, a distinctive Al-rich spinel is stable between ~1,135 and 1,035 °C, but spinel with this composition is absent at lower pressures. The olivine ($Fo_{86\text{-}84}$) appearance curve is subparallel to the Cr-spinel stability curve (liquidus), but ~40–50 °C cooler. Olivine (olv) becomes increasingly Fe-rich (to Fo_{79}) until the olivine-out curve is reached, about 150 °C cooler, again subparallel to the Cr-spinel-out curve. The appearance of pyroxenes is strongly pressure dependent, as has long been established for basalts (Yoder 1976). At 900 MPa high-Ca clinopyroxene (cpx) and orthopyroxene (opx) appear within ~35 and ~55 °C of the liquidus, but appear at progressively lower temperatures and farther below the liquidus at lower investigated pressures (Fig. 3). This trend reverses at very low pressures where the melt would exsolve nearly all its H_2O, raising the appearance temperatures of silicate minerals. Extrapolation of the opx and cpx appearance curves to higher pressures suggests that the 01SB872 composition with 2 wt% H_2O would be multiply saturated with an olv–opx–cpx-spinel assemblage at shallow subcrustal depths, consistent with it approximating a moderately hydrous near-primary peridotite partial melt. The plagioclase appearance temperature decreases with increasing pressure, first markedly from a predicted appearance at ~1,225 °C at 0.1 MPa to ~1,100 °C at 400 MPa, and then more gradually at higher pressures. As with pyroxenes, the sharp change in plagioclase appearance temperature below 400 MPa is due to low-pressure exsolution of H_2O from the melt. Magnetite crystallizes ~150 °C below the liquidus, and ilmenite crystallizes ~100 °C cooler than magnetite. The amphibole-in curve has a positive P–T slope, characteristic of hydrous phases in the lower-pressure portion of their stability fields, and occurs between 1,000 and 1,050 °C over the pressures investigated in this study.

Saturation of residual melt with a free H_2O–CO_2 vapor, along with vapor composition, were assessed with the solubility model of Papale et al. (2006), defining a vapor stability curve that is strongly sensitive to pressure below 400 MPa, but less so at higher pressures (Fig. 3). Vapor

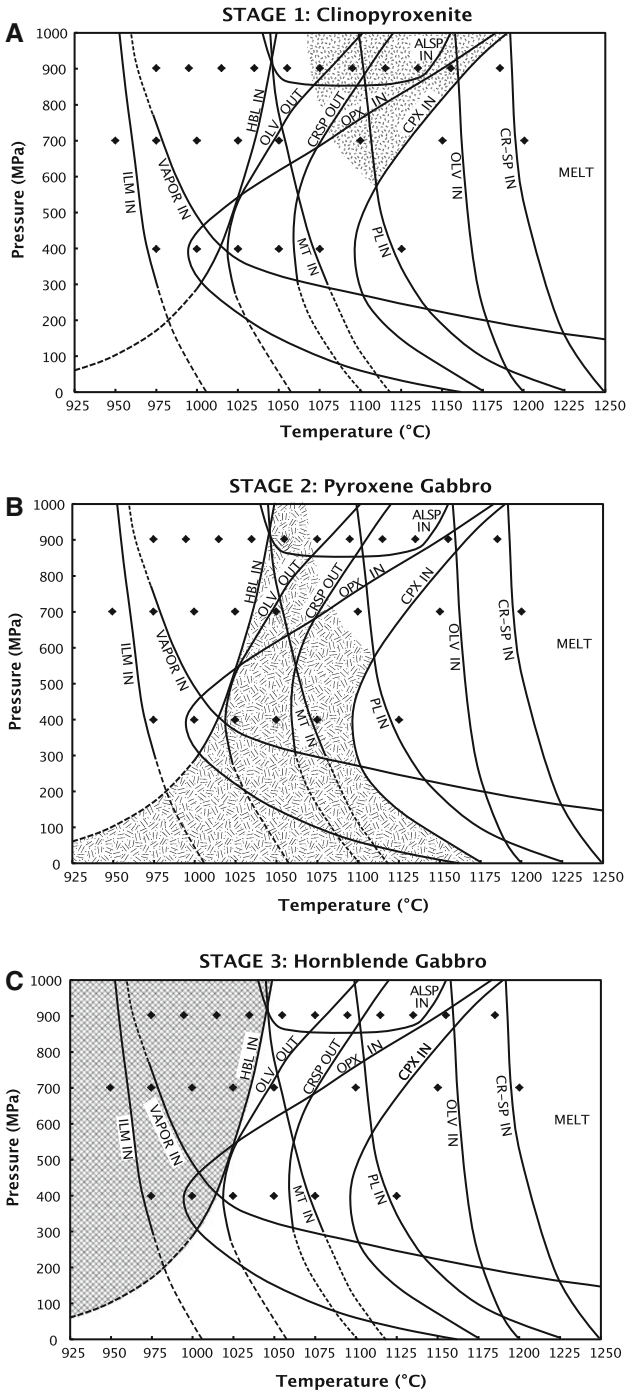

Fig. 3 Pressure–temperature diagram for basalt 01SB872 with 2 wt% H_2O near Re–ReO_2. *Black diamonds* show the P–T conditions for each experiment. *Heavy black lines* are stability boundaries for mineral phases, labeled as: *CRSP* chromium spinel, *OLV* olivine, *CPX* clinopyroxene, *OPX* orthopyroxene, *PL* plagioclase, *ALSP* aluminum spinel, *MT* magnetite, *HBL* hornblende, *ILM* ilmeno-hematite. Phase boundaries are dashed in the low P–T portion of the diagram because MELTS (Ghiorso and Sack 1995; Asimow and Ghiorso 1998) did not predict the stability of these phases at 0.1 MPa. The stability field for the mixed CO_2–H_2O vapor is calculated using Papale et al. (2006). Stages of crystallization are shown as *shaded regions* in each panel, as discussed in the text

saturation and composition were calculated by determining a nominal wt% H_2O and CO_2 of the melt by mass balance, using phase proportions and the original amount of H_2O and CO_2 in the starting material, including subtracting H_2O taken up by amphibole [modal fraction amphibole × 1.75 wt% H_2O (Dodge et al. 1968)]. These nominal melt H_2O and CO_2 concentrations were then entered into the H_2O–CO_2 solubility model (Papale et al. 2006), along with the glass composition, pressure, and temperature, yielding revised melt H_2O and CO_2 concentrations, vapor fraction, and vapor composition (Table 4). Evidence of a vapor phase was observed in 400 MPa runs as pervasive, variably sized (5–75 μm), rounded vesicles in 975 and 1,000 °C glasses (Fig. 2f), and as smaller vesicles (5–10 μm) in 1,025 °C glass, but vesicles were not found in higher temperature, more melt-rich 400 MPa runs, consistent with solubility expectations (Papale et al. 2006). Only small (1–5 μm), round, bubble-like voids are present in the low-temperature 700 MPa glasses, and none were seen at higher melt fractions or higher pressure. These small bubble-like voids are difficult to distinguish from other small sample surface irregularities and cannot be identified certainly as confirming free vapor predicted by the solubility model.

Phase descriptions

Cr-spinel forms small subhedral to euhedral equant grains (generally <5 μm, rarely to 10 μm) in the high-temperature runs at each pressure (Fig. 2b, c). The Cr#s (Cr/Cr + Al) vary from 0.43 to 0.33, with most grains having some compositional zoning from core to rim. Because the grains are small, their interiors and rims could not be analyzed separately, and average grain compositions are reported (Table 5).

Al-spinel is present only in the 900 MPa experiments as small (5 μm) euhedral grains and as rims on Cr-spinel grains in high-temperature (1,135–1,115 °C) runs. In the 1,095–1,055 °C runs, the Al-spinel forms 10 μm, euhedral grains with homogeneous compositions within each run (Fig. 2b). Near the upper and lower-temperature stability boundaries for Al-spinel, the compositions are slightly richer in FeO_T (~29–32 wt%), whereas in the other runs, the Al-spinel has 20–23 wt% FeO_T.

Olivine assumes a wide variety of shapes from large (100 μm) euhedral grains at high temperatures to small (10–20 μm) stringy blebs at low temperatures (Fig. 2a–d). Regardless of grain shape, very little compositional variation is apparent between grains or within grains of each run, and the average composition is reported in Table 5 with standard deviations for wt% MgO between <0.1 and 0.8 wt%. The forsterite (Fo) content decreases systematically with temperature, going from $Fo_{84\text{-}79}$ from 1,185 to 1,095 °C at 900 MPa, and $Fo_{85\text{-}79}$ from 1,150 to 1,050 °C at 700 MPa, and $Fo_{86\text{-}80}$ from 1,125 to 1,025 °C at 400 MPa (Table 5).

High-Ca clinopyroxene (cpx) and orthopyroxene (opx) have similar habits under most conditions where both are present. At high temperatures (1,155–1,135 °C at 900 MPa, 1,100 °C at 700 MPa, and 1,075–1,050 °C at 400 MPa), cpx grains are large (100–200 μm) and euhedral with little compositional variation within or between grains, with the exception of the highest-temperature run (2362, Fig. 2a), which contains grains that are sector zoned in Al_2O_3, CaO, and MgO. At high temperatures (1,135 °C) and 900 MPa, opx grains are large (50–100 μm), euhedral, and virtually unzoned. At 900 and 700 MPa and moderate temperatures (1,115–1,025 °C), cpx and opx form elongate (150 × 20 μm) euhedral through anhedral grains, some in glomeroporphyritic clusters with plagioclase (Fig. 2d). The low-temperature runs (below 1,025 °C at 900, 700, and 400 MPa) contain small (<50 μm), equant, euhedral to subhedral cpx and opx grains with little zoning (Fig. 2e). The average wollastonite (Wo), enstatite (En), and ferrosilite (Fs) components are reported in Table 5 and vary systematically with temperature at each pressure, except for the low-temperature runs, where abundant magnetite plus amphibole crystallization consumes Fe and increases the enstatite component.

Plagioclase forms sparse, large (75 × 300 μm), euhedral grains near its high-temperature stability limit. At moderate temperatures (1,000–1,075 °C), plagioclase forms evenly distributed, euhedral (50 × 100 μm) laths (Fig. 2c–e), which decrease in size and become subhedral to interstitial in the lowest-temperature runs (Fig. 2f). Compositional zoning is less than 1 % of the anorthite (An) component in the higher-temperature runs. Zoning increases with decreasing temperature such that the plagioclase in the lowest-temperature runs varies by up to 6 % An; their average rim compositions are reported in Table 5. Overall, the An component in the plagioclase at each pressure decreases with decreasing temperature: At 900 MPa, plagioclase spans from An_{64} at 1,095 °C to An_{50} at 975 °C; at 700 MPa, from An_{67} at 1,100 °C to An_{51} at 950 °C; and at 400 MPa from An_{72} at 1,125 °C to An_{59} at 975 °C (Table 5).

Amphibole forms 50 μm, euhedral grains near its high-temperature stability limit, but forms larger (100 μm) euhedral grains in the 900 and 700 MPa runs between 1,025 and 975 °C (Fig. 2e). At lower temperatures and pressures, the amphibole grains are <75 μm and euhedral to subhedral in habit. In the lowest-temperature run (950 °C), the amphibole forms intergrown clusters with minor opx and cpx (Fig. 2f).

Magnetite occurs as small 5–20 μm, euhedral to subhedral grains (Fig. 2c–d). The wt% FeO_T increases with decreasing temperature for each pressure investigated,

ranging from 66 to 80 wt% FeO_T (Table 5). Sparse grains of ilmenite–hematite (~21 wt% TiO_2) are present in the lowest-temperature (950 °C) experiment.

Glass in all runs is free of quench crystals, and in all experiments above 995 °C, glass forms evenly distributed pools that are at least 40 μm, with homogeneous compositions throughout each sample. Below 995 °C, melt pools can be sparse and as small as 25 μm, with more compositional heterogeneity, which is reflected in the higher reported standard deviations for the average oxide concentration in these runs, especially in sample 2370, which was run at 950 °C (Table 5).

Phase proportions

Calculated modal percentages of melt and solid phases are plotted in Fig. 4. At 900 MPa, near-liquidus crystallization is dominated by cpx + olv with trace amounts of opx, Cr-spinel, and Al-spinel. At ~1,095 °C, opx crystallization outpaces olivine, and by ~1,075 °C, olivine disappears entirely. Plagioclase precipitation begins in trace amounts at ~1,095 °C, but appears to be moderated by the occurrence of the Al-spinel phase, which is only stable together with plagioclase over a small P–T window, consistent with the experimental and modeling results of Till et al. (2012). At ~1,035 °C, when the Al-spinel disappears, plagioclase abundance sharply increases from 3 to 19 wt% and precipitation of amphibole and magnetite commence. With decreasing temperature below 1,035 °C, amphibole crystallizes at the expense of both opx and cpx, with plagioclase abundance remaining nearly constant. The melt fraction of the experiments at 900 MPa decreases systematically with decreasing temperature, except at ~1,035 °C where the melt fraction sharply declined from 60 to 33 wt%, due to the onset of amphibole crystallization. At 975 °C, as the amphibole modal percentage increases, the calculated melt fraction also increases slightly, although this is within the 8 % margin of uncertainty for the modal calculations and probably reflects a shortcoming in averaged phase compositions, or possibly a near-singularity among mineral and melt compositions that can render the least-squares approach imprecise.

At 700 MPa, olivine and Cr-spinel are joined by 15 wt% cpx and 3 wt% plagioclase at 1,100 °C. At ~1,050 °C, opx and magnetite join the assemblage and plagioclase increases from 3 to 20 wt%. Olivine disappears at 1,025 °C, and amphibole crystallization commences and markedly increases in abundance as temperature decreases, at the expense of cpx and opx. By 950 °C, ilmeno-hematite grows to trace amounts.

At 400 MPa, Cr-spinel and olivine are joined by cpx between 1,125 and 1,075 °C, and magnetite replaces Cr-spinel by 1,050 °C. At ~1,000 °C, olivine disappears and opx and amphibole crystallize. By 975 °C, amphibole abundance increases at the expense of cpx and opx.

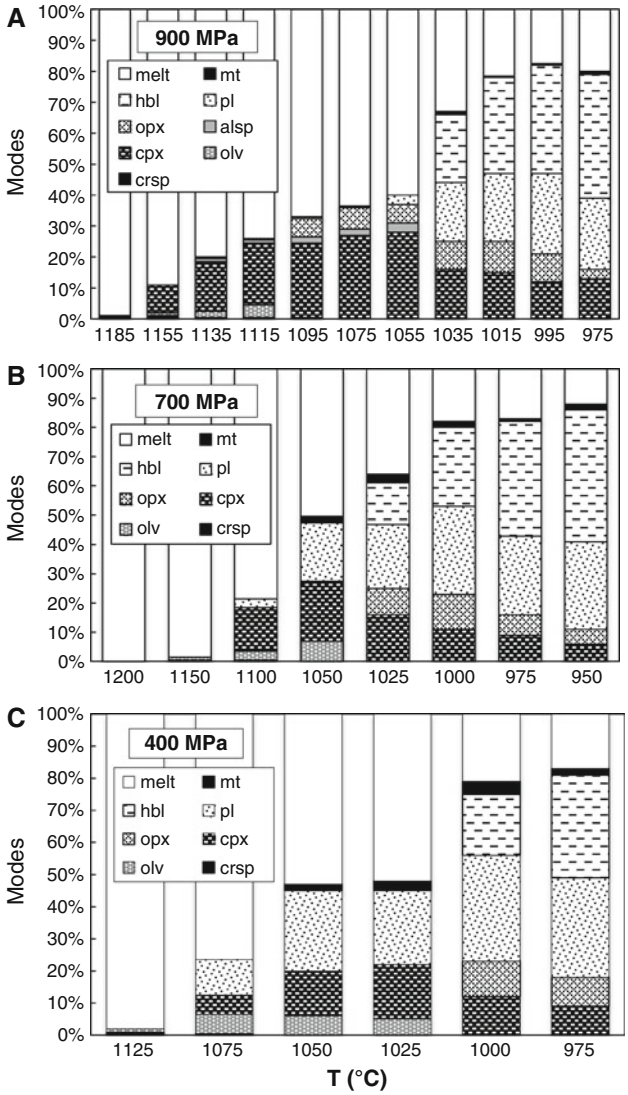

Fig. 4 Stacked bar charts showing the modal percentages of melt and crystalline phases at each temperature for 900, 700, and 400 MPa, as labeled. Phase abbreviations are as in Figs. 2 and 3

Liquid compositions

The experimental liquids produced in this study plot within the medium-K field of Gill (1981) and range from basalt to dacite (Fig. 5a). Controls on melt differentiation can be divided broadly into three stages: an early high-temperature clinopyroxenitic stage dominated by growth of clinopyroxene with subordinate olivine, orthopyroxene, and spinel (Fig. 3a); an intermediate gabbroic stage (Fig. 3b), dominated by clinopyroxene and plagioclase, joined by either Al-spinel (900 MPa) or magnetite (*s.l.*) (700, 400 MPa); and a low-temperature amphibole gabbroic stage dominated by growth of plagioclase, amphibole, and

magnetite, with concomitant resorption of early mafic silicates (Fig. 3c). The relative magnitudes of these stages vary with pressure, with the clinopyroxenitic stage diminishing and the gabbroic stage expanding, with decreasing pressure as plagioclase begins to crystallize at higher temperatures and grows in greater abundances.

These stages influence liquid differentiation paths. As temperature declines from the liquidus to ~1,100 °C, growth of abundant clinopyroxene retards the SiO_2 enrichment of derivative liquids (Fig. 6a), so that melt SiO_2 concentrations increase modestly from ~49.5 to ~51.5 wt% (melt concentrations normalized anhydrous through this section). Across this temperature interval, melt MgO concentrations decline from 8.7 to 5.5–6 wt% (higher at lower pressures) (Figs. 5d, 6d). Melt FeO* concentrations are approximately constant across the early clinopyroxene-dominated stage of crystallization (Figs. 5f, 6f), with the result that at all investigated pressures, melts increase in FeO*/MgO, but only modestly in SiO_2, so they rise short distances into the arc tholeiite field on Miyashiro's (1974) tholeiitic–calc-alkaline discriminant diagram (Fig. 5b). Melt Al_2O_3 concentrations are sensitive to the onset and abundance of plagioclase crystallization, and thus to pressure. At 900 MPa, where the near-liquidus clinopyroxenitic crystallization stage is broad, melt Al_2O_3 concentrations rise from 17 wt% at the liquidus to 20.1 wt% until the onset of plagioclase crystallization (Figs. 5e, 6c). At lower pressures, melt Al_2O_3 concentrations continue to rise into the gabbroic stage of crystallization, attaining 19.8 wt% at 700 MPa and ~18.5 wt% at 400 MPa.

The succeeding gabbroic stage of crystallization is broader at lower pressures, spanning from ~1,100 to ~1,050 °C at 900 MPa, ~1,110 to ~1,030 °C at 700 MPa, and ~1,130 to ~1,020 °C at 400 MPa (Fig. 3b). At 900 MPa, melt SiO_2 concentrations increase modestly and liquids pass from high-Al_2O_3 basalts to high-Al_2O_3 basaltic andesites. Magnetite does not appear in the gabbroic stage at that pressure, with the result that melts remain in the arc tholeiite field (Fig. 5b). Gabbroic crystallization also increases melt SiO_2 concentrations modestly at 700 and 400 MPa, but magnetite appears at progressively higher temperatures at lower pressures (Fig. 3; Table 4), with the result that at 700 and 400 MPa, melt compositions approach and intersect the tholeiitic–calc-alkaline divide (Fig. 5b). A peak in melt TiO_2 concentration of 1.5–1.7 wt% at ~1,050 °C occurs directly prior to the onset of abundant magnetite crystallization at all pressures investigated (Figs. 5h, 6h).

Amphibole grows in great abundance in the low-temperature amphibole gabbroic stage of crystallization, accompanied at all pressures by magnetite. The combined effect is to increase melt SiO_2 concentrations sharply, attaining silicic andesite values by 975 °C, and dacitic SiO_2 values at lower temperatures (Fig. 6a). At 900 MPa, amphibole gabbroic-stage liquid compositions approach and then track along the tholeiitic–calc-alkaline divide but fail to pass into the calc-alkaline field (Fig. 5b). At 700 MPa, amphibole gabbroic-stage liquid compositions cross into the calc-alkaline field, and 400 MPa liquids pass from the boundary to plot deep into the calc-alkaline field. Earlier (Fig. 3) and more abundant crystallization of magnetite (Table 4) at lower pressures probably accounts for the stronger calc-alkaline character of the lower-pressure evolved liquids, although this cannot be distinguished unambiguously from the effects of amphibole crystallization. However, the sharp increase in SiO_2 that occurs at ~1,050 °C (Fig. 6a) must be associated with magnetite crystallization in the 700 and 400 MPa liquids, since amphibole is not stable at these temperatures and pressures. An additional aspect of the amphibole gabbroic-stage liquids is that their Na_2O concentrations decline modestly with crystallization from a peak near 4.8 wt%; this exceeds the Na_2O concentrations of synthesized amphiboles (2.47–3.01 wt%), and the decline at lower temperatures probably results from combined amphibole and plagioclase growth with concurrent resorption of pyroxenes (Figs. 5g, 6g).

Although liquid compositions synthesized in this study evolve similarly to subduction zone magmas in many respects, including producing calc-alkaline types, they differ in attaining low CaO concentrations, especially at 900 and 700 MPa (Fig. 5c), due to early and abundant crystallization of clinopyroxene. Depletion of liquids in CaO during crystallization at deep-crustal conditions has been noted in the previous studies (Müntener and Ulmer 2006 and references therein) along with the observation that the low CaO concentrations lead to peraluminous (ASI: molar Al/(Na + K + 2Ca) > 1) evolved liquids. In the present study, liquids cross the metaluminous–peraluminous divide at ~61 wt% SiO_2 at 900 MPa and ~62 wt% SiO_2 at 700 MPa and do not become peraluminous at 400 MPa (Fig. 7a). Although peraluminous compositions occur in arc volcanic rocks, according to Gill (1981), only 15 % of orogenic andesites are corundum-normative. Implications of high-pressure peraluminous differentiation are addressed in the following section.

Discussion

A first-order result of this investigation is that low-MgO, high-Al_2O_3 liquids with basaltic SiO_2 concentrations can form by deep-crustal clinopyroxene-dominated crystallization of moderately hydrous magnesian arc basalts. Evolved high-Al_2O_3 basalts are widespread in some arcs and have been hypothesized to form by such deep-crustal pyroxene-

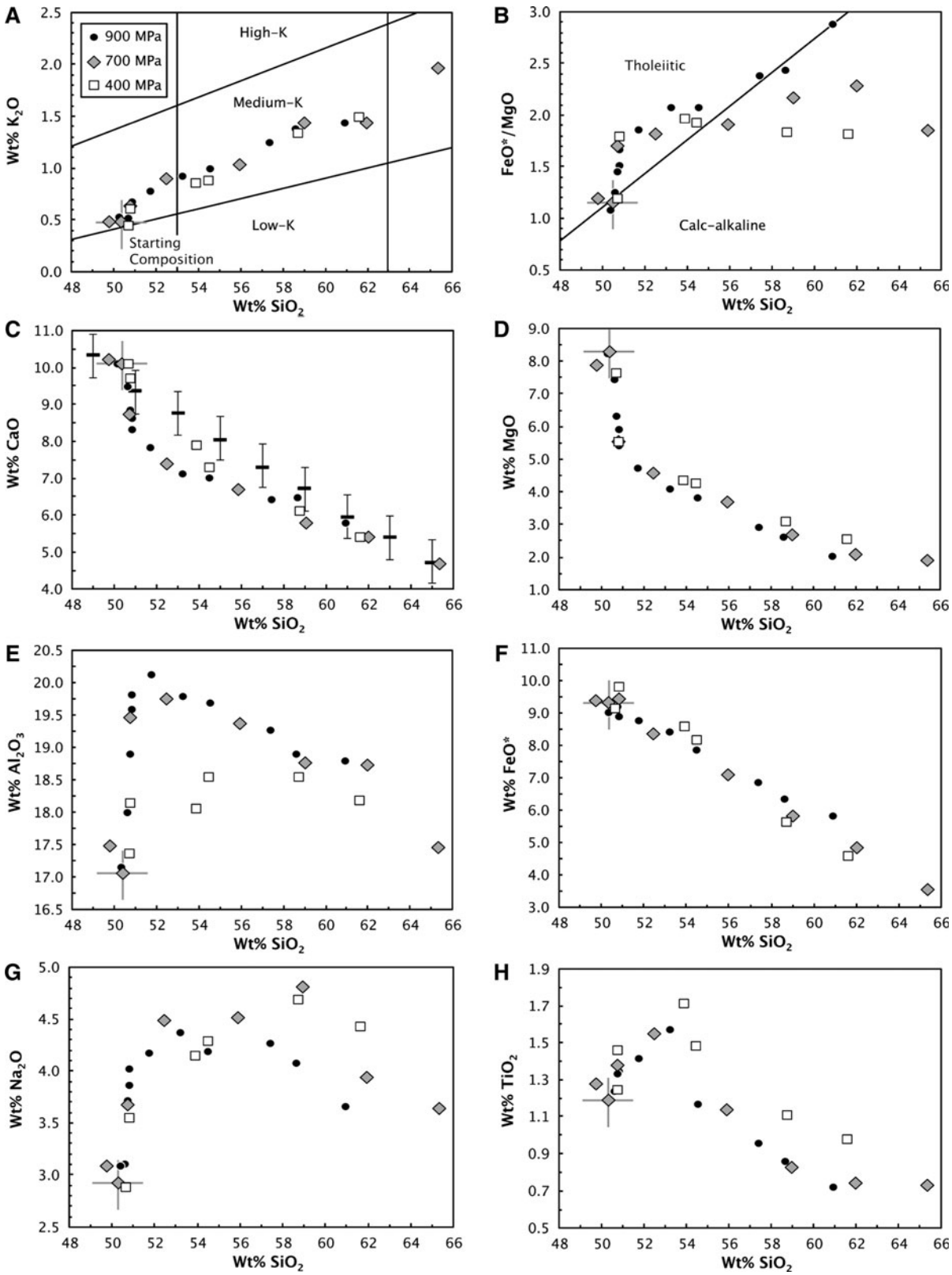

Fig. 5 Oxide concentrations of synthesized glasses, normalized anhydrous, plotted versus wt% SiO_2. The field boundaries in (**a**) are from Gill (1981) and in (**b**) from Miyashiro (1974). The CaO versus SiO_2 points plotted for the Cascades in (**c**) are derived by calculating the average CaO value for every 2 wt% SiO_2, along with one sigma standard deviation shown by uncertainty brackets on each point

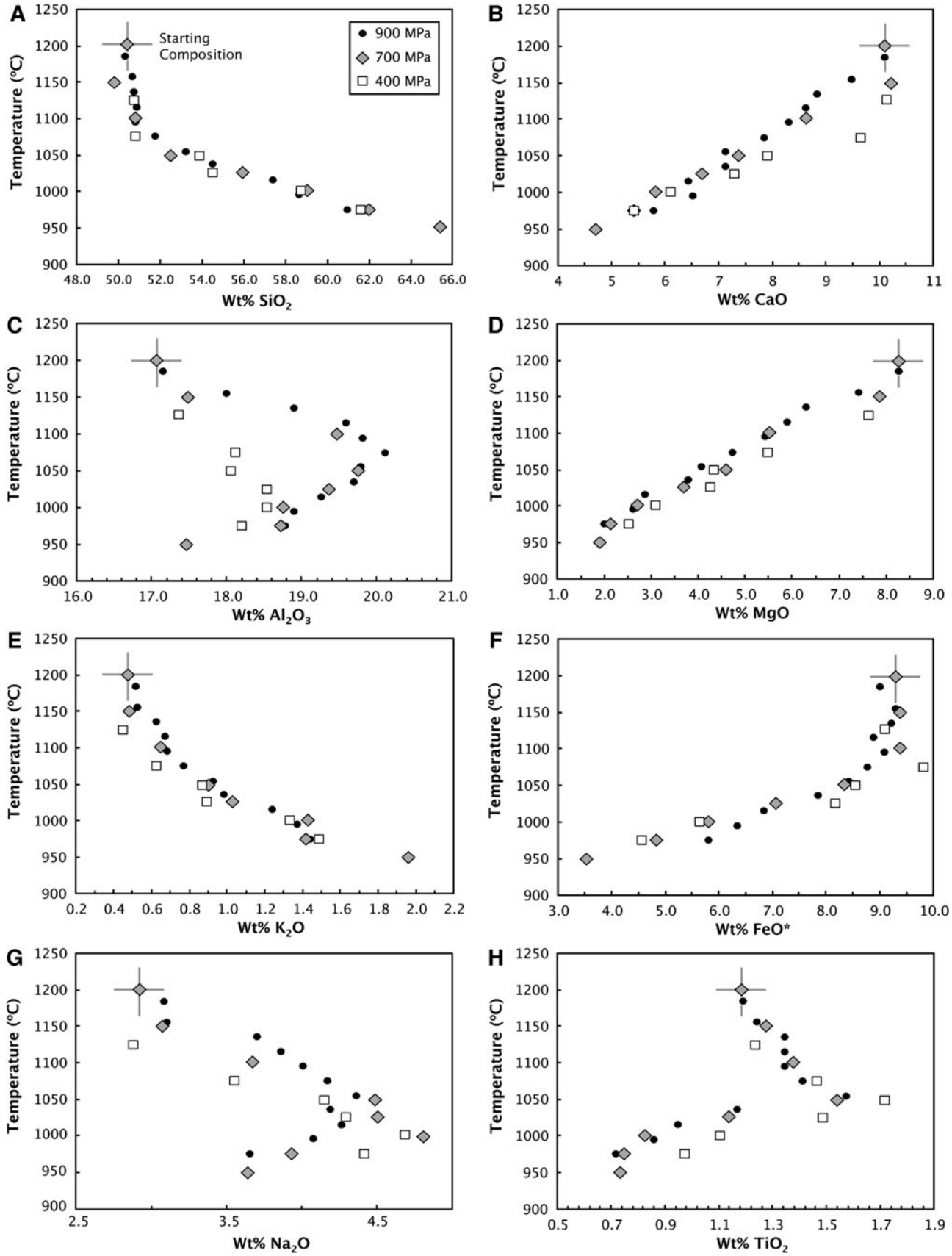

Fig. 6 Oxide concentrations of synthesized glasses, normalized anhydrous, plotted versus temperature (°C)

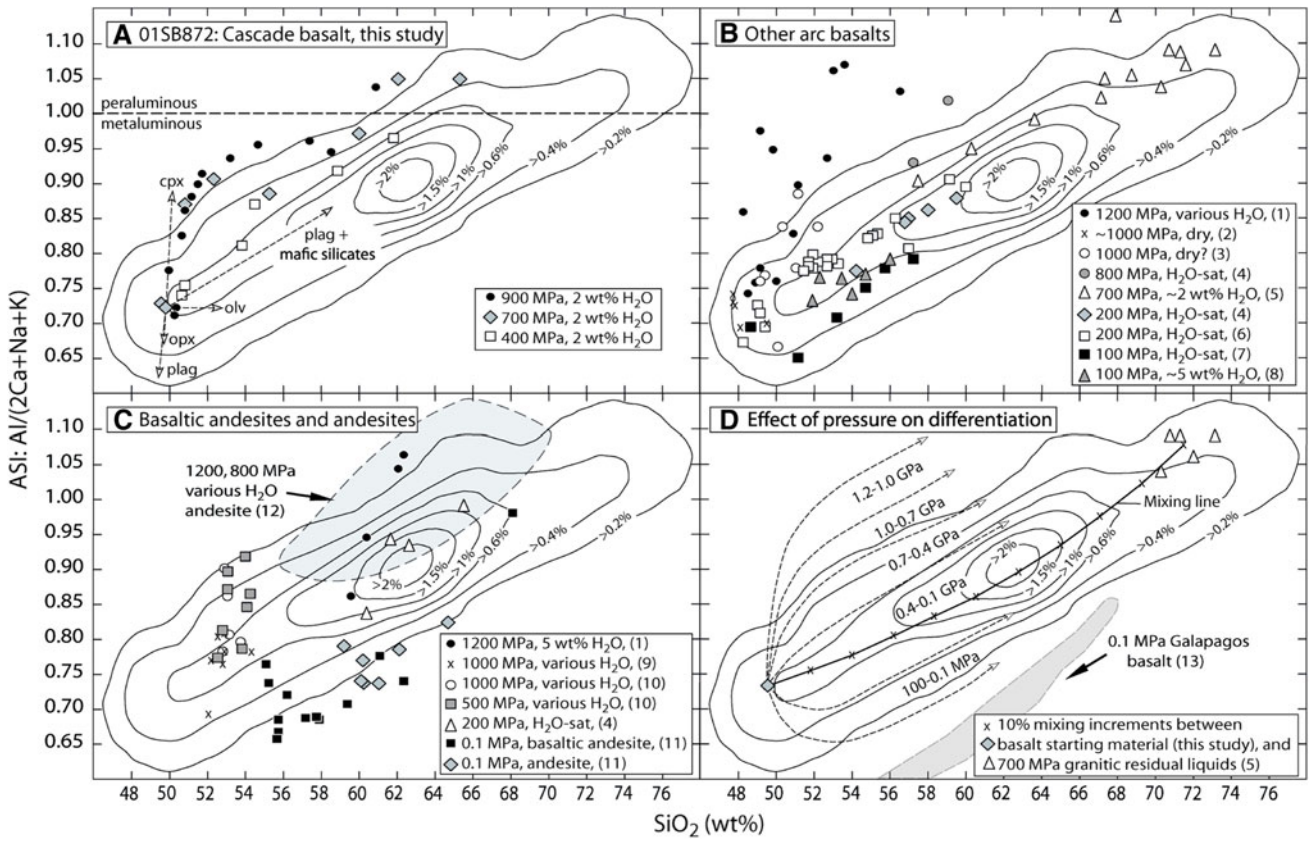

Fig. 7 Abundance density contour plot of ASI = molar Al/(2Ca + Na + K) versus SiO_2 (wt%) for >6,500 igneous rocks from the Cascades magmatic arc and Sierra Nevada batholith with experimental liquids (normalized anhydrous) plotted for comparison. Contours give the abundance density (%) of compositions plotting within each 0.025ASI X 1.0 wt% SiO_2 cells. For example, within the >2 % abundance density contour, there were more than 130 samples within each cell, whereas within the >0.2 % abundance density contour, there were only 14 samples within each cell. The peak of the abundance density contours shows that the most commonly analyzed rock for these arcs is: ~63 wt% SiO_2 with an ASI of ~0.9; however, the rocks form a compositional continuum from basalt (gabbro) to rhyolite (granite) with a corresponding range of ASI. The boundary for peraluminous compositions ASI > 1 is shown in panel **a** for reference. The experimental liquids from this study and others from the literature are shown in separate panels, divided by starting composition: **a** Rainier-area basalt (01SB872), this study. Also shown are trajectories of liquid evolution during 20 wt% crystallization of: *cpx* clinopyroxene, *plag* plagioclase, *olv* olivine, and *opx* orthopyroxene, using high-pressure phase compositions, and the general trend for crystallization of plagioclase + mafic silicates. **b** Other arc basalts and basaltic-composition gabbros from: (1) Müntener et al. (2001), (2) Bartels et al. (1991), (3) Draper and Johnston (1992), (4) Grove et al. (2003), (5) Sisson et al. (2005), (6) Sisson and Grove (1993a), (7) Sisson and Grove (1993b), and (8) Wagner et al. (1995). **c** Basaltic andesite and andesite from: (9) Weaver et al. (2011), (10) Mercer and Johnston (2008), (11) Grove and Juster (1989), and (12) Alonzo-Perez et al. (2009). The Alonzo-Perez compositions scatter widely, probably due to diverse H_2O concentrations, and are shown as a field rather than individual points, **d** Rainier-area basalt from this study shown with a mixing line to the average composition of evolved experimental liquids with >70 wt% SiO_2 produced by Sisson et al. (2005) using Sierran basaltic starting compositions. Approximate trajectories for melt evolution at various pressures are generalized from the previous plots (**a**–**c**) and shown as *dashed lines*, labeled with approximate pressures. Because H_2O concentrations differed in each study, the effects of water versus pressure on ASI versus SiO_2 cannot be fully deconvolved. A field for low-pressure (0.1 MPa) dry basalt differentiation (Juster et al. 1989) is shown for comparison with arc magmas; the lower limit of this dry, low-pressure field plots off-scale to the *lower left* of the diagram

rich crystallization processes (Sisson and Grove 1993b; Grove et al. 2003). Another result is that basalt crystallization at mid- and deep-crustal pressures readily produces liquids with andesitic and dacitic SiO_2 concentrations. Under sufficiently oxidizing conditions (>Ni–NiO), mid- to deep-crustal crystallization also produces the low FeO*/MgO characteristic of calc-alkaline magmas, consistent with earlier work on basaltic-composition gabbros at higher extents of crystallization that produced calc-alkaline rhyodacite and rhyolite liquids (Sisson et al. 2005). Development of calc-alkaline character diminishes as pressures approach those of the base of the continental crust (900 MPa), possibly due to high-pressure stabilization of Al-spinel instead of magnetite (Fig. 3).

It is widely hypothesized that primitive basalts or gabbros are rare in active arcs and in the mid- and upper

continental crust because primitive basaltic magmas commonly stall near the base of the crust, due to reduced buoyancy or enhanced heat loss. If so, and those basalts crystallized similarly to the experiments in this study, then peraluminous andesites and dacites would be widespread. They are not, however, as is shown by a compilation of >6,500 analyses of volcanic and intrusive rocks from the Cascades and the Sierra Nevada batholith. Figure 7 illustrates that ASI in these arc suites increases continuously and linearly with whole-rock SiO_2 from basalts to rhyolites or granites (ASI/wt% SiO_2 0.012–0.014). Although a modest number of arc magmas are peraluminous across a range of SiO_2 contents, the vast majority of arc compositions are not peraluminous until whole-rock SiO_2 exceeds about 69 wt%, indicating that arcs readily produce weakly peraluminous rhyodacitic and rhyolitic magmas, but do not commonly produce peraluminous andesites and dacites. In contrast to the arc suites, the 900 and 700 MPa experimental liquids from this study diverge early from the natural arc trend, with their ASIs increasing markedly with limited increases in melt SiO_2 concentration; the 400 MPa liquids do not diverge as strongly from the natural arc ASI–SiO_2 array (Fig. 7a). At all pressures investigated in this study, once plagioclase joins mafic silicates in the crystallizing assemblage, the ASI–SiO_2 trajectories of the experimental liquids shift to trending approximately parallel to the natural arc array, with the 400 MPa liquids overlapping it most closely (Fig. 7a).

Few other experimental studies publish results for crystallization–differentiation of moderately hydrous arc basalts at deep-crustal or shallow-subcrustal conditions. Those available also show prematurely peraluminous differentiates, or steep trajectories of melt ASI versus SiO_2, dissimilar to the natural arc igneous suites (Fig. 7b). Müntener et al. (2001) investigated a high-MgO basalt from the Mt. Shasta region of the California Cascades (85–44) in an experimental study that explored a range of initial H_2O concentrations: 2.5, 3.8, and 5 wt% H_2O, at 1.2 GPa and temperatures from 1,230 to 1,070 °C (Fig. 7b: black-filled circles). Cpx grew in modal abundances of ~2.8 to 31 % in all experiments, and liquids were peraluminous by the time they evolved to 54–58 wt% SiO_2 (normalized anhydrous). The evolving liquids define an initially steep trend of ASI versus SiO_2, dissimilar to the field for arc magmas from the Cascades and Sierra, clearly above the natural trend (Fig. 7b). H_2O-saturated experiments by Grove et al. (2003) explored the phase equilibria of the same basaltic composition (85–44) at 200 and 800 MPa between 1,090 and 990 °C. These experiments also report abundant crystallization of cpx (1–28 %), except in their highest P/T run, at 800 MPa and 1,090 °C, where only olivine crystallized. Their two 800 MPa liquids (normalized anhydrous) plot above the ASI versus SiO_2 array for natural arc magmas (Fig. 7b: gray circles), becoming peraluminous by ~59 wt% SiO_2. Highly crystallized, low-temperature experiments run at 700 MPa on Sierran basaltic-composition amphibole gabbros (Sisson et al. 2005) also produce liquids that are peraluminous at ≥63.5 wt% SiO_2 and yield a trend that is roughly parallel to that of natural liquids, but at higher ASI values (Fig. 7b: white triangles). In contrast, relatively low-pressure (100, 200 MPa) H_2O-saturated experiments on basaltic compositions (Sisson and Grove 1993a, b; Grove et al. 2003; Wagner et al. 1995) produce liquids that evolve similar to the array of natural arc magmas (Fig. 7b: white squares, black squares, gray diamonds, and gray triangles, respectively). The distinguishing feature of these relatively low-pressure experiments is that abundant plagioclase accompanies olivine and clinopyroxene (or amphibole) in the near-liquidus crystallizing assemblages, moderating the increase in melt ASI with increasing SiO_2.

Several studies (Baker et al. 1994; Hirose and Kawamoto 1995; Hirose 1997; Blatter and Carmichael 2001; Grove et al. 2003, 2006; Straub et al. 2008, 2011) propose basaltic andesite or high-MgO andesite as a common parental magma type in arcs, rather than basalt. Experiments on a low-MgO, high-alumina basaltic andesite from North Sister Volcano, Oregon Cascades, at pressures of 500 and 1,000 MPa and H_2O concentrations of 0, 3.5, 5, 10, and 15 wt% (Mercer and Johnston 2008), show that near-liquidus melts fractionate along steep ASI versus SiO_2 trends (Fig. 7c: white circles and gray squares), even though the liquid fraction in those experiments was never less than 90 wt%. This steep trend is consistent with the low abundances of plagioclase in the earliest crystallizing assemblages, as well as augite crystallization at higher H_2O concentrations. Experimental investigation of a high-MgO basaltic andesite at the pressure of 1,000 MPa and H_2O of 3–7 wt% (Weaver et al. 2011) produced orthopyroxene as the dominant near-liquidus crystallizing phase, which would not be expected to change liquid ASI appreciably, yet the initial trajectory is also steep (Fig. 7c: black x's). Alonzo-Perez et al. (2009) conducted high-pressure (1,200–800 MPa) experiments on a synthetic andesite at H_2O concentrations of 4, 6, and 8 wt% and noted that the liquids became peraluminous at ≥61 wt% SiO_2, depending on water concentrations (Fig. 7c: gray field). High-pressure (1,200 MPa) experiments on a high-MgO andesite from the Mt. Shasta region, Cascades (Müntener et al. 2001), show that crystallization of this composition also produces a steep ASI versus SiO_2 melt trend similar to crystallizing basalt or basaltic andesite (Fig. 7c: black-filled circles). In contrast, lower-pressure (200 MPa), H_2O-saturated experiments on the same composition (Grove et al. 2003) indicate that the melt ASI versus SiO_2 trend is within the range

of natural arc magmas (Fig. 7c: white triangles). For comparison, basaltic andesite and andesite crystallized at 0.1 MPa (Grove and Juster 1989) produce evolved liquids that skirt the lower boundary of ASI versus SiO_2 for natural magmas (Fig. 7c: black squares and gray diamonds).

Nominally dry basalts experimentally crystallized at deep- or shallow-crustal conditions generally saturate early with plagioclase, and thus, their liquids define shallower trajectories of ASI versus SiO_2, more similar to the natural arc suites. Nominally dry liquids produced at 1,000 MPa from a primitive Cascades high-Al_2O_3 basalt from near Mount Shasta define an ASI/SiO_2 slope that is slightly negative (decreasing SiO_2: black x's in Fig. 7b), although the trajectory is not well defined due to a narrow temperature range investigated below the liquidus (Bartels et al. 1991). Plagioclase did not saturate early in the crystallization sequence of a high-MgO Aleutian basalt that was also considered to be nominally dry (Draper and Johnston 1992), and the experimental liquids follow a steep ASI/SiO_2 trajectory similar to those of wet high-MgO basalt (Fig. 7b: white circles), consistent with the inferences by Weaver et al. (2011) that the starting material of Draper and Johnston (1992) contained modest H_2O.

General observations from these experimental studies are that for basalts, basaltic andesites, and andesites with H_2O concentrations appropriate for arc magmas, (1) clinopyroxene crystallizes early and in abundance at deep-crustal and subcrustal pressures, driving intermediate liquids to ASI values greater than for common arc magmas, (2) melt trajectories produced by co-crystallization of plagioclase plus mafic silicates are similar to the ASI versus SiO_2 array defined by arc magmas, and (3) increasing pressure of crystallization shifts melt differentiation paths to higher ASI values. Crystallization at atmospheric pressure produces evolved liquids with ASI values at or below the limit of the natural arc array (Fig. 7c, d), whereas crystallization at deep-crustal and subcrustal pressures produces evolved liquids with ASI values greater than the natural arc array (Fig. 7a, b), including producing peraluminous andesitic liquids that are rare in nature. The shift to higher ASI is intrinsically tied to the overall proportion of plagioclase versus mafic silicates that crystallize, so there is not a one-to-one relation between pressure and differentiation path. Other compositional factors being equal, magma with a higher H_2O concentration would have reduced plagioclase stability and so would differentiate at higher ASI for the same pressure. Despite these ambiguities, the overall effect of pressure on differentiation trajectory can be sketched schematically (Fig. 7d) and shows that the preponderance of arc magma compositions matches plagioclase plus mafic silicate differentiation paths at mid- to upper-crustal pressures. Certainly, progressive differentiation of primitive basalts in the deep crust or uppermost mantle does not dominate production of the arc magmatic suite.

Several inferences could be drawn from the similarity between mid- to upper-crustal liquid lines of descent and typical arc magma compositions (Fig. 7): (1) Primitive arc basalts may commonly reach and differentiate at shallow crustal depths. However, the scarcity of gabbroic cumulates, primitive lavas, and primitive dikes in the upper arc crust weighs against this interpretation. (2) The compositions investigated in this and other experimental studies could be inappropriate, with the true parents being richer in normative plagioclase or poorer in H_2O than those studied, so that plagioclase would saturate early in the deep crust. The basalt composition investigated here is not atypical, however (Fig. 7), and H_2O even less than 2 wt% would contradict the preponderance of arc basaltic melt inclusion analyses (Métrich and Wallace 2008), so this interpretation is also not favored. A variant of this hypothesis is that basaltic andesites are the common parental magmas in arcs, and these might crystallize abundant orthopyroxene in the deep crust, which would not increase melt ASI or SiO_2 significantly. Deep-crustal crystallization behavior of basaltic andesites is not well explored experimentally, so this possibility remains open, but the hypothesis fails to account for the compositional continuity of basalts with the rest of the arc magmatic suite. Finally, (3) it may be that open-system processes outweigh progressive crystallization–differentiation in the production of arc magmatic suites. One possibility is that primitive basalts stall in the deep crust and solidify to large degrees, leaving highly evolved granitic or rhyolitic residual liquids (Sisson et al. 2005), and these then mix into subsequent basalt injections, drawing them along the arc ASI versus SiO_2 array (Fig. 7d). Silicic liquids could also derive by low-degree partial melting of earlier intrusions and of unrelated country rocks. Assimilation of partly degassed residual liquids, and degassed intrusions and their partial melts, could limit or reduce melt H_2O concentrations, thereby accounting for the intermediate H_2O concentrations of melt inclusions in andesites and dacites (Wallace 2005). Low H_2O due to assimilation or mixing could also potentially force early plagioclase crystallization in the deep crust, promoting differentiation along the arc ASI versus SiO_2 array.

The relations shown in Fig. 7 also have implications for understanding the processes that created the continents. If the andesitic or dacitic bulk composition of the continents derived from source materials similar to modern arc basalts, the mafic component lost to the mantle would lie along the arc ASI–SiO_2 trajectory, either at its low-SiO_2 end or projected to even lower SiO_2 values. Such rocks would be gabbroic in composition, not clinopyroxenites or orthopyroxenites. In keeping with option 3 in the preceding paragraph, producing melt-depleted plagioclase-bearing mafic

residues at deep-crustal pressures is accomplished most readily by either high degrees of basalt crystallization or low degrees of partial melting, accompanied by silicic melt extraction. The residual rocks would be gabbros and would be buoyant relative to peridotite, so post-magmatic cooling into the eclogite facies, or collisional events depressing the residual gabbros into the eclogite facies, in both cases followed by eclogite delamination (Jull and Kelemen 2001), may be necessary aspects of continent differentiation.

Conclusions

Experimental crystallization of moderately hydrous, oxidized, magnesian arc basalt at deep to mid-crustal pressures reproduces many aspects of subduction zone magmas, including (1) generation of high-Al_2O_3, low-MgO basalts and basaltic andesites by deep-crustal crystallization of pyroxene, (2) the subsequent production of melts with andesitic and dacitic SiO_2 concentrations, as well as other features similar to arc magmas, and (3) the low FeO*/MgO ratios characteristic of calc-alkaline andesites and dacites due to both magnetite and amphibole crystallization. Deep-crustal melt compositions differ, however, from common natural arc magmas in attaining peraluminous compositions at andesitic or dacitic SiO_2 concentrations, with the peraluminous character developing more strongly and appearing earlier in the differentiation process at higher pressures. These results imply that to maintain the metaluminous character of the overwhelming majority of arc magmas, the spectrum of typical arc magmas is produced by either: (1) chiefly mid- to upper-crustal fractional crystallization or remelting of basaltic compositions or (2) mixing of mafic magmas with evolved crustal melts or residual liquids in the deep crust, forcing plagioclase saturation, and causing coupled and consistent increase in SiO_2 with ASI. Alternatively, and equally controversial, it may be that parental arc basalts generally have less than 2 wt% H_2O and are more similar to back-arc basin basalts than is generally accepted.

Acknowledgments The authors thank Jim Brophy, Christy Till, and an anonymous reviewer for insightful comments that helped improve this manuscript. Additional comments and editorial handling by Gordon Moore are also appreciated. Conversations with Peter Ulmer and Othmar Müntener, while looking at rocks in the Sierra Nevada, helped stimulate this project. Robert Oscarson and Leslie Hayden provided assistance with probe analyses at the USGS Electron Microprobe Facility in Menlo Park, CA. Jake Lowenstern provided guidance with the FTIR analyses and provided the calibration equations for ATR-FTIR analyses prior to publication. Joel Robinson provided help with the density contour plot. This research was supported by the USGS Volcano Hazards Program. The first author would also like to acknowledge the generous mentorship and friendship of the late Ian Carmichael, to whom this volume is dedicated. Not a day goes by without the thought: "What would Ian say about this?" as a litmus test to any method, idea, or decision. Thank you Ian!

References

Alonzo-Perez R, Müntener O, Ulmer P (2009) Igneous garnet and amphibole fractionation in the roots of island arcs: experimental constraints on andesitic liquids. Contrib Mineral Petrol 157:541–558. doi:10.1007/s00410-008-0351-8

Asimow PD, Ghiorso MS (1998) Algorithmic modifications extending MELTS to calculate subsolidus phase relations. Am Mineral 83(9–10):1127–1132

Bacon CR, Bruggman PE, Christiansen RL, Clynne MA, Donnelly-Nolan JM, Hildreth W (1997) Primitive magmas at five Cascade volcanic fields; melts from hot, heterogeneous sub-arc mantle. Can Mineral 35(2):397–423

Baker MB, Grove TL, Price R (1994) Primitive basalts and andesites from the Mt. Shasta region, N. California: products of varying melt fraction and water content. Contrib Mineral Petrol 118:111–129. doi:10.1007/BF01052863

Balta JB, Beckett JR, Asimow PD (2011) Thermodynamic properties of alloys of gold-74/palladium-26 with variable amounts of iron and the use of Au–Pd–Fe alloys as containers for experimental petrology. Am Mineral 96(10):1467–1474. doi:10.2138/am.2011.3637

Bartels K, Kinzler R, Grove T (1991) High pressure phase relations of primitive high-alumina basalts from Medicine Lake volcano, northern California. Contrib Mineral Petrol 108(3):253–270. doi:10.1007/bf00285935

Blatter DL, Carmichael ISE (2001) Hydrous phase equilibria of a Mexican high-silica andesite: a candidate for a mantle origin? Geochim Cosmochim Acta 65(21):4043–4065. doi:10.1016/s0016-7037(01)00708-6

Bohlen SR, Boettcher AL (1982) The quartz-coesite transformation: a precise determination and the effects of other components. J Geophys Res 87(B8):7073–7078. doi:10.1029/JB087iB08p07073

Botcharnikov RE, Almeev RR, Koepke J, Holtz F (2008) Phase relations and liquid lines of descent in hydrous ferrobasalt—implications for the skaergaard intrusion and Columbia River flood basalts. J Petrol 49(9):1687–1727. doi:10.1093/petrology/egn043

Bowen NL (1928) The evolution of igneous rocks. Princeton University Press, New Jersey

Boyd FR, England JL (1960) Apparatus for phase-equilibrium measurements at pressures up to 50 kilobars and temperatures up to 1750°C. J Geophys Res 65(2):741–748. doi:10.1029/JZ065i002p00741

Carmichael ISE (1991) The redox states of basic and silicic magmas: a reflection of their source regions? Contrib Mineral Petrol 106(2):129–141. doi:10.1007/bf00306429

Chou IM (1978) Calibration of oxygen buffers at elevated P and T using the hydrogen fugacity sensor. Am Mineral 63:690–703

DePaolo DJ (1980) Crustal growth and mantle evolution: inferences from models of element transport and Nd and Sr isotopes. Geochim Cosmochim Acta 44(8):1185–1196. doi:10.1016/0016-7037(80)90072-1

DePaolo DJ (1981) Trace element and isotopic effects of combined wallrock assimilation and fractional crystallization. Earth Planet Sci Lett 53(2):189–202. doi:10.1016/0012-821x(81)90153-9

Dixon JE, Pan V (1995) Determination of the molar absorptivity of dissolved carbonate in basanitic glass. Am Mineral 80:1339–1342

Dixon JE, Stolper EM, Holloway JR (1995) An experimental study of water and carbon dioxide solubilities in mid-ocean ridge basaltic liquids. Part I: calibration and solubility models. J Petrol 36(6):1607–1631

Dodge FCW, Papike JJ, Mays RE (1968) Hornblendes from granitic rocks of the central Sierra Nevada Batholith, California. J Petrol 9(3):378–410. doi:10.1093/petrology/9.3.378

Draper DS, Johnston AD (1992) Anhydrous PT phase relations of an Aleutian high-MgO basalt: an investigation of the role of

olivine-liquid reaction in the generation of arc high-alumina basalts. Contrib Mineral Petrol 112(4):501–519. doi:10.1007/bf00310781

Eugster HP (1957) Heterogeneous reactions involving oxidation and reduction at high pressures and temperatures. J Chem Phys 26(6):1760. doi:10.1063/1.1743626

Faure F, Schiano P (2005) Experimental investigation of equilibration conditions during forsterite growth and melt inclusion formation. Earth Planet Sci Lett 236:882–898. doi:10.1016/j.epsl.2005.04.050

Ghiorso MS, Sack RO (1995) Chemical mass transfer in magmatic processes IV. A revised and internally consistent thermodynamic model for the interpolation and extrapolation of liquid-solid equilibria in magmatic systems at elevated temperatures and pressures. Contrib Mineral Petrol 119(2):197–212. doi:10.1007/bf00307281

Gill JB (1981) Orogenic andesites and plate tectonics. Springer-Verlag, New York

Grove TL, Juster TC (1989) Experimental investigations of low-Ca pyroxene stability and olivine-pyroxene-liquid equilibria at 1-atm in natural basaltic and andesitic liquids. Contrib Mineral Petrol 103:287–305

Grove TL, Elkins-Tanton LT, Parman SW, Chatterjee N, Müntener O, Gaetani GA (2003) Fractional crystallization and mantle-melting controls on calc-alkaline differentiation trends. Contrib Mineral Petrol 145(5):515–533. doi:10.1007/s00410-003-0448-z

Grove TL, Chatterjee N, Parman SW, Médard E (2006) The influence of H_2O on mantle wedge melting. Earth Planet Sci Lett 249:74–89

Hansen M, Anderko K (1958) Constitution of binary alloys. McGraw-Hill, New York

Hirose K (1997) Melting experiments on lherzolite KLB-1 under hydrous conditions and generation of high-magnesian andesitic melts. Geology 25:42–44

Hirose K, Kawamoto T (1995) Hydrous partial melting of lherzolite at 1 GPa: the effect of H_2O on the genesis of basaltic magmas. Earth Planet Sci Lett 133:463–473

Jull M, Kelemen PB (2001) On the conditions for lower crustal convective instability. J Geophys Res 106(B4):6423–6446. doi:10.1029/2000JB900357

Juster TC, Grove TL, Perfit MR (1989) Experimental constraints on the generation of FeTi basalts, andesites and rhyodacites at the Galapagos Spreading Center, 85°W and 95°W. J Geophys Res 94:9251–9274

Kay RW (1978) Aleutian magnesian andesites: melts from subducted Pacific Ocean crust. J Volcanol Geotherm Res 4(1–2):117–132. doi:10.1016/0377-0273(78)90032-x

Kelemen P (1986) Assimilation of ultramafic rock in subduction-related magmatic arcs. J Geol 94(6):829–843

Kelley KA, Cottrell E (2009) Water and the oxidation state of subduction zone magmas. Science 325(5940):605–607. doi:10.1126/science.1174156

Kushiro I (1974) Melting of hydrous upper mantle and possible generation of andesitic magma: an approach from synthetic systems. Earth Planet Sci Lett 22(4):294–299. doi:10.1016/0012-821x(74)90138-1

Lee C-TA, Leeman WP, Canil D, Li Z-XA (2005) Similar V/Sc systematics in MORB and arc basalts: implications for the oxygen fugacities of their mantle source regions. J Petrol 46(11):2313–2336. doi:10.1093/petrology/egi056

Lowenstern JB, Pitcher BW (2013) Analysis of H_2O in silicate glass using attenuated total reflectance (ATR) micro-FTIR spectroscopy. Amer Mineral (in press)

MacPherson CG, Dreher ST, Thirlwall MF (2006) Adakites without slab melting: high pressure differentiation of island arc magma, Mindanao, the Philippines. Earth Planet Sci Lett 243(3–4):581–593. doi:10.1016/j.epsl.2005.12.034

Martin H, Smithies RH, Rapp R, Moyen JF, Champion D (2005) An overview of adakite, tonalite–trondhjemite–granodiorite (TTG), and sanukitoid: relationships and some implications for crustal evolution. Lithos 79(1–2):1–24. doi:10.1016/j.lithos.2004.04.048

Mercer CN, Johnston AD (2008) Experimental studies of the *P-T*-H_2O near-liquidus phase relations of basaltic andesite from north sister volcano, high Oregon Cascades: constraints on lower-crustal mineral assemblages. Contrib Mineral Petrol 155:571–592. doi:10.1007/s00410-007-0259-8

Métrich N, Wallace PJ (2008) Volatile abundances in basaltic magmas and their degassing paths tracked by melt inclusions. Rev Mineral Geochem 69(1):363–402. doi:10.2138/rmg.2008.69.10

Miyashiro A (1974) Volcanic rock series in island arcs and active continental margins. Am J Sci 274(4):321–355. doi:10.2475/ajs.274.4.321

Morgan GBV, London D (1996) Optimizing the electron microprobe analysis of hydrous alkali aluminosilicate glasses. Am Mineral 81(9–10):1176–1185

Müntener O, Ulmer P (2006) Experimentally derived high-pressure cumulates from hydrous arc magmas and consequences for the seismic velocity structure of lower arc crust. Geophys Res Lett 33(21):L21308. doi:10.1029/2006gl027629

Müntener O, Kelemen P, Grove T (2001) The role of H_2O during crystallization of primitive arc magmas under uppermost mantle conditions and genesis of igneous pyroxenites: an experimental study. Contrib Mineral Petrol 141(6):643–658. doi:10.1007/s004100100266

Ochs FA, Lange RA (1999) The density of hydrous magmatic liquids. Science 283(5406):1314–1317. doi:10.1126/science.283.5406.1314

Osborn EF (1959) Role of oxygen pressure in the crystallization and differentiation of basaltic magma. Am J Sci 257:609–647

Papale P, Moretti R, Barbato D (2006) The compositional dependence of the saturation surface of H_2O–CO_2 fluids in silicate melts. Chem Geol 229(1–3):78–95. doi:10.1016/j.chemgeo.2006.01.013

Pownceby MI, O'Neill HSC (1994) Thermodynamic data from redox reactions at high temperatures. IV. Calibration of the Re–ReO_2; oxygen buffer from EMF and NiO + Ni–Pd redox sensor measurements. Contrib Mineral Petrol 118(2):130–137. doi:10.1007/bf01052864

Ringwood AE (1974) The petrological evolution of island arc systems. J Geol Soc 130(3):183–204. doi:10.1144/gsjgs.130.3.0183

Roeder PL, Emslie RF (1970) Olivine-liquid equilibrium. Contrib Mineral Petrol 29:275–289

Rudnick RL, Gao S (2003) The composition of the continental crust. In: Rudnick RL, Holland HD, Turekian KK (eds) The crust: treatise on geochemistry, vol 3. Elsevier-Pergamon, Oxford, pp 1–64

Ruscitto DM, Wallace PJ, Johnson ER, Kent AJR, Bindeman IN (2010) Volatile contents of mafic magmas from cinder cones in the Central Oregon High Cascades: implications for magma formation and mantle conditions in a hot arc. Earth Planet Sci Lett 298(1–2):153–161. doi:10.1016/j.epsl.2010.07.037

Sakuyama M (1981) Petrological Study of the Myoko and Kurohime volcanoes, Japan: crystallization sequence and evidence for magma mixing. J Petrol 22(4):553–583. doi:10.1093/petrology/22.4.553

Shaw S, DeBari SM, Wallace PJ, Sisson TW, Rowe M (2011) Volatile contents in olivine-hosted melt inclusions from primitive magmas in the northern Cascade arc. In: American Geophysical Union, Fall Meeting, vol Abstract #V41D-2526

Sisson TW, Grove TL (1993a) Experimental investigations of the role of H_2O in calc-alkaline differentiation and subduction zone magmatism. Contrib Mineral Petrol 113(2):143–166. doi:10.1007/bf00283225

Sisson TW, Grove TL (1993b) Temperatures and H_2O contents of low-MgO high-alumina basalts. Contrib Mineral Petrol 113(2):167–184. doi:10.1007/bf00283226

Sisson TW, Layne GD (1993) H_2O in basalt and basaltic andesite glass inclusions from four subduction-related volcanoes. Earth

Planet Sci Lett 117(3–4):619–635. doi:10.1016/0012-821x(93)90107-k

Sisson TW, Ratajeski K, Hankins WB, Glazner AF (2005) Voluminous granitic magmas from common basaltic sources. Contrib Mineral Petrol 148(6):635–661. doi:10.1007/s00410-004-0632-9

Stern CR, Kilian R (1996) Role of the subducted slab, mantle wedge and continental crust in the generation of adakites from the Andean austral volcanic zone. Contrib Mineral Petrol 123(3):263–281. doi:10.1007/s004100050155

Stolper E, Newman S (1994) The role of water in the petrogenesis of Mariana trough magmas. Earth Planet Sci Lett 121(3–4):293–325. doi:10.1016/0012-821x(94)90074-4

Stormer JC Jr, Nicholls J (1978) XLFRAC: a program for the interactive testing of magmatic differentiation models. Comput Geosci 4(2):143–159. doi:10.1016/0098-3004(78)90083-3

Straub SM, LaGatta AB, Martin-Del Pozzo AL, Langmuir CH (2008) Evidence from high-Ni olivines for a hybridized peridotite/pyroxenite source for orogenic andesites from the central Mexican Volcanic Belt. Geochem Geophys Geosyst 9(3):Q03007. doi:10.1029/2007gc001583

Straub SM, Gomez-Tuena A, Stuart FM, Zellmenr GF, Espinasa-Perena R, Cai Y, Iizuka Y (2011) Formation of hybrid arc andesites beneath thick continental crust. Earth Planet Sci Lett 303:337–347. doi:10.1016/j.epsl.2011.01.013

Tatsumi Y (2005) The subduction factory: how it operates in the evolving Earth. GSA Today 15:4–10

Tatsumi Y, Suzuki T (2009) Tholeiitic versus calc-alkalic differentiation and evolution of arc crust: constraints from melting experiments on a basalt from the Izu–Bonin–Mariana arc. J Petrol 50(8):1575–1603. doi:10.1093/petrology/egp044

Thorpe RS (1982) Andesites: orogenic andesites and related rocks. Wiley, Chichester

Till CB, Grove TL, Krawczynski MJ (2012) A melting model for variably depleted and enriched lherzolite in the plagioclase and spinel stability fields. J Geophys Res 117:B06206. doi:10.1029/2011JB009044

Toplis MJ (2005) The thermodynamics of iron and magnesium partitioning between olivine and liquid: criteria for assessing and predicting equilibrium in natural and experimental systems. Contrib Mineral Petrol 149(1):22–39. doi:10.1007/s00410-004-0629-4

Wagner TP, Donnelly-Nolan JM, Grove TL (1995) Petrogenesis of low-MgO, high Al_2O_3 basalt and basaltic andesite: the roles of hydrous differentiation and crystal accumulation. Contrib Mineral Petrol 121:201–216

Wallace PJ (2005) Volatiles in subduction zone magmas: concentrations and fluxes based on melt inclusion and volcanic gas data. J Volcanol Geotherm Res 140(1–3):217–240. doi:10.1016/j.jvolgeores.2004.07.023

Weaver SL, Wallace PJ, Johnston AD (2011) A comparative study of continental versus intraoceanic arc mantle melting: experimentally determined phase relations of hydrous primitive melts. Earth Planet Sci Lett 308:97–106. doi:10.1016/j.epsl.2011.05.040

Wood BJ, Fraser DG (1976) Elementary thermodynamics for geologists. Oxford University Press, Oxford

Wysolcazanski R, Tani K (2006) Spectographic FTIR imaging of water species in silicic volcanic glasses and melt inclusions: an example form the Izu–Bonin arc. J Volcanol Geotherm Res 156:302–314. doi:10.1016/j.jvolgeores.2006.03.024

Yoder HS (1976) Generation of basaltic magma. National Academy of Science, Washington, DC

Zimmer MM, Plank T, Hauri EH, Yogodzinski GM, Stelling P, Larsen J, Singer B, Jicha B, Mandeville C, Nye CJ (2010) The role of water in generating the calc-alkaline trend: new volatile data for Aleutian magmas and a new tholeiitic index. J Petrol 51(12):2411–2444. doi:10.1093/petrology/egq062